A&A 541, A94 (2012)
DOI: 10.1051/0004-6361/201118743

Astronomy & Astrophysics

"TNOs are Cool": A survey of the trans-Neptunian region

VI. *Herschel*⋆/PACS observations and thermal modeling of 19 classical Kuiper belt objects

E. Vilenius[1], C. Kiss[2], M. Mommert[3], T. Müller[1], P. Santos-Sanz[4], A. Pal[2], J. Stansberry[5], M. Mueller[6,7], N. Peixinho[8,9], S. Fornasier[4,10], E. Lellouch[4], A. Delsanti[11], A. Thirouin[12], J. L. Ortiz[12], R. Duffard[12], D. Perna[13,14], N. Szalai[2], S. Protopapa[15], F. Henry[4], D. Hestroffer[16], M. Rengel[17], E. Dotto[13], and P. Hartogh[17]

[1] Max-Planck-Institut für extraterrestrische Physik, Postfach 1312, Giessenbachstr., 85741 Garching, Germany
e-mail: vilenius@mpe.mpg.de
[2] Konkoly Observatory of the Hungarian Academy of Sciences, 1525 Budapest, PO Box 67, Hungary
[3] Deutsches Zentrum für Luft- und Raumfahrt e.V., Institute of Planetary Research, Rutherfordstr. 2, 12489 Berlin, Germany
[4] LESIA-Observatoire de Paris, CNRS, UPMC Univ. Paris 06, Univ. Paris-Diderot, France
[5] Stewart Observatory, The University of Arizona, Tucson AZ 85721, USA
[6] SRON LEA/HIFI ICC, Postbus 800, 9700AV Groningen, The Netherlands
[7] UNS-CNRS-Observatoire de la Côte d'Azur, Laboratoire Cassiopée, BP 4229, 06304 Nice Cedex 04, France
[8] Center for Geophysics of the University of Coimbra, Av. Dr. Dias da Silva, 3000-134 Coimbra, Portugal
[9] Astronomical Observatory of the University of Coimbra, Almas de Freire, 3040-04 Coimbra, Portugal
[10] Univ. Paris Diderot, Sorbonne Paris Cité, 4 rue Elsa Morante, 75205 Paris, France
[11] Laboratoire d'Astrophysique de Marseille, CNRS & Université de Provence, 38 rue Frédéric Joliot-Curie, 13388 Marseille Cedex 13, France
[12] Instituto de Astrofísica de Andalucía (CSIC), Camino Bajo de Huétor 50, 18008 Granada, Spain
[13] INAF – Osservatorio Astronomico di Roma, via di Frascati, 33, 00040 Monte Porzio Catone, Italy
[14] INAF – Osservatorio Astronomico di Capodimonte, Salita Moiariello 16, 80131 Napoli, Italy
[15] University of Maryland, College Park, MD 20742, USA
[16] IMCCE, Observatoire de Paris, 77 Av. Denfert-Rochereau, 75014 Paris, France
[17] Max-Planck-Institut für Sonnensystemforschung, Max-Planck-Straße 2, 37191 Katlenburg-Lindau, Germany

Received 25 December 2011 / Accepted 6 March 2012

ABSTRACT

Context. Trans-Neptunian objects (TNO) represent the leftovers of the formation of the solar system. Their physical properties provide constraints to the models of formation and evolution of the various dynamical classes of objects in the outer solar system.
Aims. Based on a sample of 19 classical TNOs we determine radiometric sizes, geometric albedos and beaming parameters. Our sample is composed of both dynamically hot and cold classicals. We study the correlations of diameter and albedo of these two subsamples with each other and with orbital parameters, spectral slopes and colors.
Methods. We have done three-band photometric observations with *Herschel*/PACS and we use a consistent method for data reduction and aperture photometry of this sample to obtain monochromatic flux densities at 70.0, 100.0 and 160.0 μm. Additionally, we use *Spitzer*/MIPS flux densities at 23.68 and 71.42 μm when available, and we present new *Spitzer* flux densities of eight targets. We derive diameters and albedos with the near-Earth asteroid thermal model (NEATM). As auxiliary data we use reexamined absolute visual magnitudes from the literature and data bases, part of which have been obtained by ground based programs in support of our *Herschel* key program.
Results. We have determined for the first time radiometric sizes and albedos of eight classical TNOs, and refined previous size and albedo estimates or limits of 11 other classicals. The new size estimates of 2002 MS_4 and 120347 Salacia indicate that they are among the 10 largest TNOs known. Our new results confirm the recent findings that there are very diverse albedos among the classical TNOs and that cold classicals possess a high average albedo (0.17 ± 0.04). Diameters of classical TNOs strongly correlate with orbital inclination in our sample. We also determine the bulk densities of six binary TNOs.

Key words. Kuiper belt: general – infrared: planetary systems – techniques: photometric

1. Introduction

The physical properties of small solar system bodies offer constraints on theories of the formation and evolution of the planets. Trans-Neptunian objects (TNO), also known as Kuiper belt objects (KBO), represent the leftovers from the formation period of the outer solar system (Morbidelli et al. 2008), and they are analogues to the parent bodies of dust in debris disks around other stars (Wyatt 2008; Moro-Martín et al. 2008, and references therein).

In addition to Pluto more than 1400 TNOs have been discovered since the first KBO in 1992 (Jewitt & Luu 1993), and the current discovery rate is 10 to 40 new TNOs/year. The dynamical

⋆ *Herschel* is an ESA space observatory with science instruments provided by European-led Principal Investigator consortia and with important participation from NASA.

classification is based on the current short-term dynamics. We use the classification of Gladman (Gladman et al. 2008, 10 Myr time-scale): classical TNOs are those non-resonant TNOs which do not belong to any other TNO class. The classical TNOs are further divided into the main classical belt, the inner belt ($a < 39.4$ AU) and the outer belt ($a > 48.4$ AU). The eccentricity limit for classicals is $e < 0.24$, beyond which targets are classified as detached or scattered objects. The classification scheme of the Deep Eplictic Survey team (DES, Elliot et al. 2005) differs from the Gladman system in terms of the boundary of classical and scattered objects, which do not show a clear demarcation in their orbital parameters. Some of the classicals in the Gladman system are scattered-near or scattered-extended in the DES system. Another division is made in the inclination/eccentricity space. Although there is no dynamical separation, there seems to be two distinct but partly overlapping inclination distributions with the low-i "cold" classicals, limited to the main classical belt, showing different average albedo (Grundy et al. 2005; Brucker et al. 2009), color (Trujillo & Brown 2002), luminosity function (Fraser et al. 2010), and frequency of binary systems (Noll et al. 2008) than the high-i "hot" classicals, which has a wider inclination distribution. Furthermore, models based on recent surveys suggest that there is considerable sub-structure within the main classical belt (Petit et al. 2011). To explain these differences more quantitative data on physical size and surface composition are needed.

The physical characterization of TNOs has been limited by their large distance and relatively small sizes. Accurate albedos help to correctly interpret spectra and are needed to find correlations in the albedo-size-color-orbital parameters space that trace dynamical and collisional history. The determination of the size frequency distribution (SFD) of TNOs provides one constraint to formation models and gives the total mass. The SFD of large bodies is dominated by accretion processes and they hold information about the angular momentum of the pre-solar nebula whereas bodies smaller than 50 to 100 km are the result of collisional evolution (Petit et al. 2008). The SFD can be estimated via the luminosity function (LF), but this size distribution also depends on assumptions made about surface properties such as albedo. Consequently, ambiguities in the size distributions derived from the LFs of various dynamical classes are one significant reason why there is a wide uncertainty in the total TNO mass estimate ranging from 0.01 $M_{\rm Earth}$ (Bernstein et al. 2004) to 0.2 $M_{\rm Earth}$ (Chiang et al. 1999). Among the formation models of our solar system the "Nice" family of models have been successful in explaining the orbits of planets and the formation of the Kuiper belt (Tsiganis et al. 2005; Levison et al. 2008), although they have difficulties in explaining some of the details of the cold and hot distributions and the origin of the two sub-populations (e.g. Fraser et al. 2010; Petit et al. 2011; Batygin et al. 2011).

Only a few largest TNOs have optical size estimates based on direct imaging and assumptions about the limb darkening function (e.g. Quaoar, Fraser & Brown 2010). The combination of optical and thermal infrared observations gives both sizes and geometric albedos, but requires thermal modeling. Earlier results from *Spitzer* and *Herschel* have shown the usefulness of this method (e.g. Stansberry et al. 2008; Müller et al. 2010) and significantly changed the size and albedo estimates of several TNOs compared to those obtained by using an assumed albedo.

In this work we present new radiometric diameters and geometric albedos for 19 classical TNOs. Half of them have no previously published observations in the wavelength regime used in this work. Those which have been observed before by *Spitzer* now have more complete sampling of their spectral energy distributions (SEDs) close to the thermal peak. The new estimates of the 19 targets are based on observations performed with the ESA *Herschel* Space Observatory (Pilbratt et al. 2010) and its Photodetector Array Camera and Spectrometer (PACS; Poglitsch et al. 2010). Other *Herschel* results for TNOs have been presented by Müller et al. (2010), Lellouch et al. (2010) and Lim et al. (2010). New estimates of 18 Plutinos are presented in Mommert et al. (2012) and of 15 scattered disc and detached objects in Santos-Sanz et al. (2012).

This paper is organized in the following way. We describe our target sample in Sect. 2.1, *Herschel* observations in Sect. 2.2 and *Herschel* data reduction in Sect. 2.3. New or re-analyzed flux densities from *Spitzer* are presented in Sect. 2.4. As auxiliary data we use absolute V-band magnitudes (Sect. 2.5), which we have adopted from other works or data bases taking into account the factors relevant to their uncertainty estimates. Thermal modeling is described in Sect. 3 and the results for individual targets in Sect. 4. In Sect. 5 we discuss sample properties of our sample and of all classicals with radiometric diameters and geometric albedos as well as correlations (Sect. 5.1) and the bulk densities of binaries (Sect. 5.2). Finally, the conclusions are in Sect. 6.

2. Observations and data reduction

Our sample of 19 TNOs has been observed as part of the *Herschel* key program "TNOs are Cool" (Müller et al. 2009) mainly between February and November 2010 by the photometry sub-instrument of PACS in the wavelength range 60–210 μm.

2.1. Target sample

The target sample consists of both dynamically cold and hot classicals (Table 1). We use a cut-off limit of $i = 4.5°$ in illustrating the two subsamples. Another typical value used in the literature is $i = 5°$. The inclination limit is lower for large objects (Petit et al. 2011) which have a higher probability of belonging to the hot population. Targets 119951 (2002 KX_{14}), 120181 (2003 UR_{292}) and 78799 (2002 XW_{93}) are in the inner classical belt and are therefore considered to belong to the low-inclination tail of the hot population. The latter two would be Centaurs in the DES system and all targets in Table 1 with $i > 15°$ would belong to the scattered-extended class of DES.

The median absolute V-magnitudes (H_V, see Sect. 2.5) of our sample are 6.1 mag for the cold sub-sample and 5.3 mag for the hot one. Levison & Stern (2001) found that bright classicals have systematically higher inclinations than fainter ones. This trend is seen among our targets (see Sect. 5.1.3). Another known population characteristics is the lack of a clear color demarcation line at $i \approx 5°$ (Peixinho et al. 2008), which is absent also from our sample of 10 targets with known colors.

2.2. Herschel observations

PACS is an imaging dual band photometer with a rectangular field of view of $1.75' \times 3.5'$ with full sampling of the 3.5 m-telescope's point-spread function (PSF). The two detectors are bolometer arrays, the short-wavelength one has 64×32 pixels and the long-wavelength one 32×16 pixels. In addition, the short-wavelength array has a filter wheel to select between two bands: 60−85 μm or 85−125 μm, whereas the long-wavelength band is 125−210 μm. In the PACS photometric system these bands have been assigned the reference wavelengths

Table 1. Target sample.

Target	KBO location	a [a] (AU)	q (AU)	i [a] (°)	e [a]	Color [b]	Spectral slope (% /100 nm)	H_V (mag)
119951 (2002 KX_{14})	inner	38.9	37.1	0.4	0.05	RR-IR[c]	27.1 ± 1.0[e]	4.862 ± 0.038[r]
(2001 XR_{254})*	main	43.0	41.7	1.2	0.03	...	10 ± 3[f]	6.030 ± 0.017[s]
275809 (2001 QY_{297})*	main	44.0	40.4	1.5	0.08	BR	24 ± 8[f,g,h]	6.09 ± 0.03[f]
(2001 RZ_{143})*	main	44.4	41.3	2.1	0.07	...	13 ± 6[h,i,j]	6.69 ± 0.10[i]
(2002 GV_{31})	main	43.9	40.0	2.2	0.09	...	...	H_R = 5.5[t] ±0.4
79360 Sila (1997 CS_{29})*	main	43.9	43.4	2.2	0.01	RR	27.0 ± 3.0[e]	5.59 ± 0.06[f,u]
88611 Teharonhiawako (2001 QT_{297})*	main	44.2	43.2	2.6	0.02	...	1 ± 2[f]	5.97 ± 0.03[f]
120181 (2003 UR_{292})	inner	32.6	26.8	2.7	0.18	...	28 ± 5[k]	H_R = 6.7[t] ±0.3
(2005 EF_{298})	main	43.9	40.1	2.9	0.09	RR	...	H_R = 5.8[t] ±0.3
138537 (2000 OK_{67})	main	46.8	40.0	4.9	0.14	RR	20 ± 3[h,j,l,m,n]	6.47 ± 0.09[l,m]
148780 Altjira (2001 UQ_{18})*	main	44.5	41.8	5.2	0.06	RR	35 ± 6[f,g,h,j]	6.47 ± 0.13[f,g]
(2002 KW_{14})	main	46.5	37.3	9.8	0.20	...	...	5.88 ± 0.05[v]
(2001 KA_{77})	main	47.3	42.8	11.9	0.10	RR	38 ± 3[g,h,j,m,o]	5.64 ± 0.08[g]
19521 Chaos (1998 WH_{24})	main	46.0	41.1	12.0	0.11	IR	23 ± 2[h,j,m,n,p,q]	4.97 ± 0.05[g,u]
78799 (2002 XW_{93})	inner	37.6	28.3	14.3	0.25	...	...	H_R = 4.8[t] ±0.6
(2002 MS_4)	main	41.7	35.6	17.7	0.15	...	2 ± 2[k]	H_R = 3.5[t] ±0.4
145452 (2005 RN_{43})	main	41.8	40.6	19.2	0.03	RR-IR[c]	23.0 ± 1.1[e]	3.89 ± 0.05[v]
90568 (2004 GV_9)	main	41.8	38.7	22.0	0.07	BR[d]	15 ± 3[k]	4.25 ± 0.04[w]
120347 Salacia (2004 SB_{60})*	main	42.2	37.9	23.9	0.10	...	12.6 ± 2.0[e]	4.26 ± 0.02[f]

Notes. Semimajor axis a, perihelion distance q, inclination i, eccentricity e, color taxonomy, spectral slope, and the average absolute visual magnitudes (V or R-band) of 19 TNOs ordered according to increasing inclination. For H_V used in our analysis, see Table 5. The horizontal line marks the limit of dynamically cold and hot classicals according to our dynamical analysis using the Gladman system. * Denotes a known binary system (Noll et al. 2008).

References. [(a)] IAU Minor Planet Center, URL: http://www.minorplanetcenter.net/iau/Ephemerides/Distant/, accessed July 2011. [(b)] Taxonomic class from Fulchignoni et al. (2008) unless otherwise indicated. [(c)] Barucci et al. (2011). [(d)] Perna et al. (2010). [(e)] Fornasier et al. (2009). [(f)] Benecchi et al. (2009). [(g)] Doressoundiram et al. (2005). [(h)] Calculated using the technique of Hainaut & Delsanti (2002). [(i)] Santos-Sanz et al. (2009). [(j)] Values from the Minor Bodies in the Outer solar system data base, URL: http://www.eso.org/~ohainaut/MBOSS. [(k)] Stephen Tegler (priv. comm.). [(l)] Benecchi et al. (2011). [(m)] Doressoundiram et al. (2002). [(n)] Delsanti et al. (2001). [(o)] Peixinho et al. (2004). [(p)] Barucci et al. (2000). [(q)] Tegler & Romanishin (2000). [(r)] Rabinowitz et al. (2007). [(s)] Grundy et al. (2009). [(t)] IAU Minor Planet Center/List of Transneptunian Objects at URL http://www.minorplanetcenter.net/iau/lists/TNOs.html accessed June 2011. See Sect. 2.5 for conversion to H_V. [(u)] Romanishin & Tegler (2005). [(v)] Perna et al. (in prep.). [(w)] DeMeo et al. (2009).

70.0 μm, 100.0 μm and 160.0 μm and they have the names "blue", "green" and "red". Both bolometers are read-out at 40 Hz continuously and binned by a factor of four on-board.

We specified the PACS observation requests (AOR) using the scan-map Astronomical Observation Template (AOT) in HSpot, a tool provided by the *Herschel* Science Ground Segment Consortium. The scan-map mode was selected due to its better overall performance compared to the point-source mode (Müller et al. 2010). In this mode the pointing of the telescope is slewed at a constant speed over parallel lines, or "legs". We used 10 scan legs in each AOR, separated by 4″. The length of each leg was 3.0′, except for Altjira where it was 2.5′, and the slewing speed was 20″ s^{-1}. Each one of these maps was repeated from two to five times.

To choose the number of repetitions, i.e. the duration of observations, for our targets we used the Standard Thermal Model (see Sect. 3) to predict their flux densities in the PACS bands. Based on earlier *Spitzer* work (Stansberry et al. 2008) we adopted a geometric albedo of 0.08 and a beaming parameter of 1.25 for observation planning purposes. The predicted thermal fluxes depend on the sizes, which are connected to the assumed geometric albedo and the absolute V-magnitudes via Eq. (3). In some cases the absolute magnitudes used for planning purposes are quite different (by up to 0.8 mag) from those used for modeling our data as more recent and accurate visible photometry was taken into account (see Sect. 2.5).

The PACS scan-map AOR allows the selection of either the blue or green channel; the red channel data are taken simultaneously whichever of those is chosen. The sensitivity of the blue channel is usually limited by instrumental noise, while the red channel is confusion-noise limited (PACS AOT release note 2010). The sensitivity in the green channel can be dominated by either source, depending on the depth and the region of the sky of the observation. For a given channel selection (blue or green) we grouped pairs of AORs, with scan orientations of 70° and 110° with respect to the detector array, in order to make optimal use of the rectangular shape of the detector. Thus, during a single visit of a target we grouped 4 AORs to be observed in sequence: two AORs in different scan directions and this repeated for the second channel selection.

The timing of the observations, i.e. the selection of the visibility window, has been optimized to utilize the lowest far-infrared confusion noise circumstances (Kiss et al. 2005) such that the estimated signal-to-noise ratio due to confusion noise has its maximum in the green channel. Each target was visited twice with similar AORs repeated in both visits for the purpose of background subtraction. The timing of the second visit was calculated such that the target has moved 30−50″ between the visits so that the target position during the second visit is within the high-coverage area of the map from the first visit. Thus, we can determine the background for the two source positions.

The observational details are listed in Table 2. All of the targets observed had predicted astrometric 3σ uncertainties

Table 2. Individual observations of the sample of 19 TNOs by *Herschel*/PACS.

Target	OBSIDs	Duration (min)	Mid-time	r (AU)	Δ (AU)	α (°)
119951 (2002 KX_{14})	1342205144-5147	59.8	26-Sep.-2010 21:52:54	39.3993	39.8605	1.30
119951 (2002 KX_{14})	1342205175-5178	59.8	27-Sep.-2010 15:35:54	39.3993	39.8716	1.29
(2001 XR_{254})	1342205184-5187	78.6	27-Sep.-2010 18:48:10	44.1004	44.4032	1.25
(2001 XR_{254})	1342205264-5267	78.6	28-Sep.-2010 15:48:21	44.1004	44.3886	1.25
(2001 QY_{297})	1342209492-9495	97.4	18-Nov.-2010 10:06:17	43.2452	43.3599	1.31
(2001 QY_{297})	1342209650-9653	97.4	19-Nov.-2010 20:50:15	43.2455	43.3850	1.31
(2001 RZ_{143})	1342199503-9506	97.4	01-Jul.-2010 00:52:31	41.3006	41.6947	1.31
(2001 RZ_{143})	1342199614-9617	97.4	01-Jul.-2010 20:28:08	41.3005	41.6819	1.32
(2002 GV_{31})	1342198847-8850	59.8	20-Jun.-2010 20:07:56	40.2818	40.5238	1.42
(2002 GV_{31})	1342198897-8900	59.8	21-Jun-2010 21:55:30	40.2817	40.5412	1.41
79360 Sila[a]	1342187073	94.4	18-Nov.-2009 14:24:02	43.5090	43.2410	1.27
79360 Sila	1342196137-6140	59.8	09-May-2010 01:29:23	43.5057	43.6530	1.33
79360 Sila	1342196137-6140	59.8	10-May-2010 09:15:12	43.5057	43.6753	1.32
88611 Teharonhiawako	1342196099-6102	78.6	09-May-2010 22:19:55	45.0856	45.3612	1.24
88611 Teharonhiawako	1342196145-6148	78.6	10-May-2010 18:30:58	45.0857	45.3475	1.25
120181 (2003 UR_{292})	1342199618-9621	59.8	01-Jul.-2010 21:49:00	26.7872	27.1477	2.04
120181 (2003 UR_{292})	1342199646-9649	59.8	02-Jul.-2010 12:43:03	26.7872	27.1379	2.05
(2005 EF_{298})	1342208962-8965	97.4	03-Nov.-2010 20:07:09	40.7207	41.1758	1.25
(2005 EF_{298})	1342208999-9002	97.4	04-Nov.-2010 10:08:12	40.7207	41.1667	1.25
138537 (2000 OK_{67})	1342197665-7668	78.6	03-Jun.-2010 00:55:51	40.3008	40.3581	1.46
138537 (2000 OK_{67})	1342197717-7720	78.6	04-Jun.-2010 13:55:32	40.3006	40.3319	1.46
148780 Altjira	1342190917-0920	76.0	21-Feb.-2010 23:32:17	45.5387	45.5571	1.25
148780 Altjira	1342191120-1123	76.0	24-Feb.-2010 01:31:06	45.5390	45.5940	1.25
(2002 KW_{14})	1342204196-4199	59.8	09-Sep.-2010 11:11:36	40.8385	41.0710	1.38
(2002 KW_{14})	1342204282-4285	59.8	10-Sep.-2010 09:37:01	40.8389	41.0870	1.38
(2001 KA_{77})	1342205962-5965	78.6	06-Oct.-2010 21:09:43	48.1789	48.6245	1.07
(2001 KA_{77})	1342206013-6016	78.6	07-Oct.-2010 14:32:45	48.1787	48.6354	1.07
19521 Chaos	1342202285-2288	41.0	08-Aug.-2010 19:40:03	41.6914	42.1566	1.24
19521 Chaos	1342202316-2319	41.0	09-Aug.-2010 11:34:49	41.6913	42.1464	1.25
78799 (2002 XW_{93})	1342190913-0916	57.8	21-Feb.-2010 22:20:43	44.6271	44.3163	1.22
78799 (2002 XW_{93})	1342191116-1119	57.8	24-Feb.-2010 00:19:32	44.6279	44.3518	1.23
(2002 MS_4)	1342204140-4143	41.0	08-Sep.-2010 21:12:31	47.1673	46.9025	1.19
(2002 MS_4)	1342204292-4295	41.0	10-Sep.-2010 15:03:37	47.1670	46.9307	1.20
145452 (2005 RN_{43})	1342195583-5586	41.0	25-Apr.-2010 22:21:44	40.6885	41.1522	1.26
145452 (2005 RN_{43})	1342195600-5603	41.0	26-Apr.-2010 21:43:12	40.6885	41.1378	1.28
90568 (2004 GV_9)	1342202869-2872	41.0	11-Aug.-2010 18:35:31	39.1876	39.3841	1.46
90568 (2004 GV_9)	1342202921-2924	41.0	12-Aug.-2010 15:22:58	39.1877	39.3984	1.46
120347 Salacia	1342199133-9136	41.0	22-Jun.-2010 01:17:20	44.1464	44.0169	1.33
120347 Salacia	1342199133-9136	41.0	22-Jun.-2010 18:57:52	44.1466	44.0058	1.32

Notes. OBSIDs are the observation identifiers, duration is the total duration of the four AORs (see text), mid-time is the mean UT time, r is the mean heliocentric distance, Δ is the mean *Herschel*-target distance, and α is the mean phase angle. Each line corresponds to one visit and all three channels were observed at each visit. r, Δ and α are from the JPL Horizons Ephemeris System (Giorgini et al. 1996). [(a)] Observation in the chopped and nodded point-source mode and only at the blue and red channels (Müller et al. 2010).

less than 10″ at the time of the *Herschel* observations (David Trilling, priv. comm.).

2.3. Data reduction

The data reduction from level 0 (raw data) to level 2 (maps) was done using *Herschel* Interactive Processing Environment (HIPE[1]) with modified scan-map pipeline scripts optimized for the "TNOs are Cool" key program. The individual maps (see Fig. 1 for examples) from the same epoch and channel are mosaicked, and background-matching and source-stacking techniques are applied. The two visits are combined (Fig. 2), in each of the three bands, and the target with a known apparent motion is located at the center region of these maps. The detector pixel sizes are 3.2″ × 3.2″ in the blue and green channels, and 6.4″ × 6.4″ in the red channel whereas the pixel sizes in the maps produced by this data reduction are 1.1″/1.4″/2.1″ in the blue/green/red maps, respectively. A detailed description of the data reduction in the key program is given in Kiss et al. (in prep.).

Once the target is identified we measure the flux densities at the photocenter position using DAOPHOT routines (Stetson 1987) for aperture photometry. We make a correction for the encircled energy fraction of a point source (PACS photometer PSF 2010) for each aperture used. We try to choose the optimum aperture radius in the plateau of stability of the growth-curves, which is typically 1.0–1.25 times the full-width-half-maximum of the PSF (5.2″/7.7″/12.0″ in the blue/green/red bands, respectively). The median aperture radius for targets in the "TNOs are Cool" program is 5 pixels in the final

[1] Data presented in this paper were analysed using "HIPE", a joint development by the *Herschel* Science Ground Segment Consortium, consisting of ESA, the NASA *Herschel* Science Center, and the HIFI, PACS and SPIRE consortia members, see http://herschel.esac.esa.int/DpHipeContributors.shtml

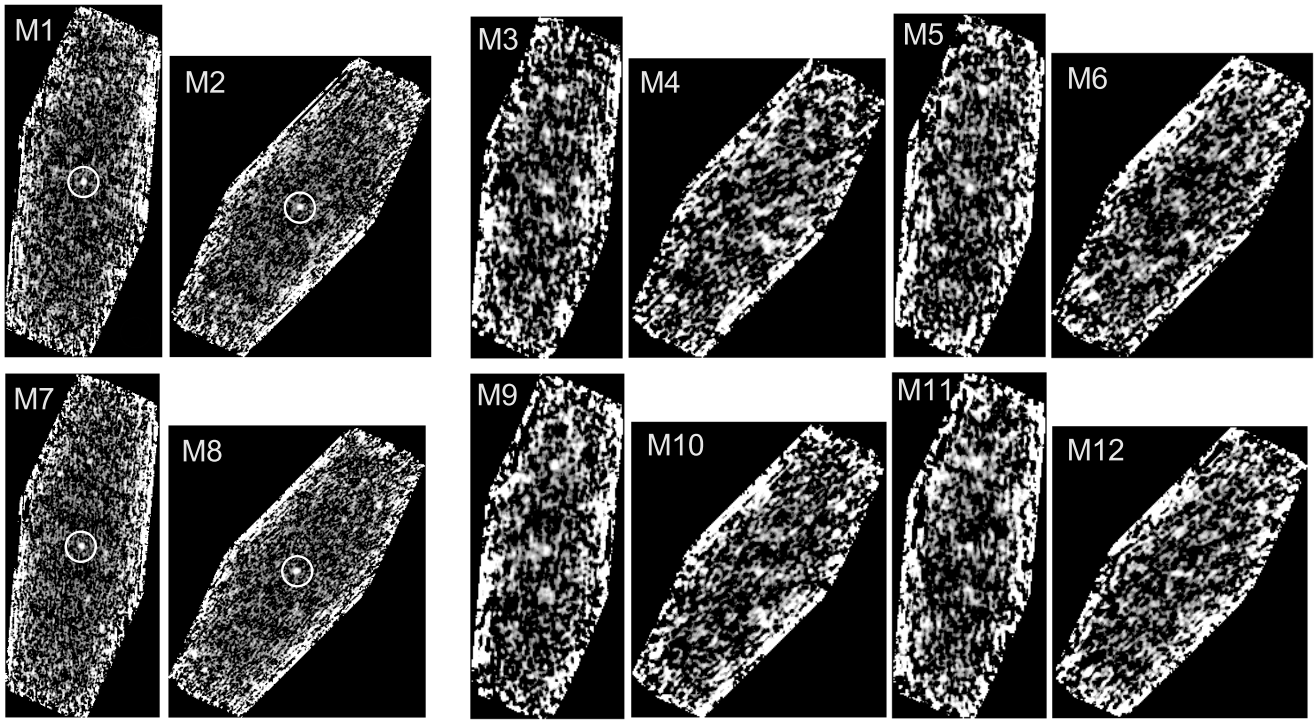

Fig. 1. Individual maps of 120347 Salacia. Each map is the product of one observation (AOR). The first row (M1-M6) is from the first visit and the second row (M7-M12) from the follow-on visit. The first two columns (M1-M2, M7-M8) are observations in the 100 μm or "green" channel and the others in the 160 μm or "red" channel. The two scan angles are 110° (odd-numbered maps) and 70°. The source is clearly seen in the map center in the green channel whereas the red channel is more affected by background sources and confusion noise. Orientation: north is up and east is to the left.

maps (pixel sizes 1.1″/1.4″/2.1″ in the blue/green/red maps). For the uncertainty estimation of the flux density we implant 200 artificial sources in the map in a region close to the source (<50″) excluding the target itself. A detailed description of how aperture photometry is implemented in our program is given in Santos-Sanz et al. (2012).

In order to obtain monochromatic flux density values of targets having a SED different from the default one color corrections are needed. In the photometric system of the PACS instrument *flux density* is defined to be the flux density that a source with a flat spectrum (λF_λ = const., where λ is the wavelength and F_λ is the monochromatic flux) would have at the PACS reference wavelengths (Poglitsch et al. 2010). Instead of the flat default spectrum we use a cool black body distribution to calculate correction coefficients for each PACS band. The filter transmission and bolometer response curves needed for this calculation are available from HIPE, and we take as black body temperature the disk averaged day-side temperature calculated iteratively for each target ($\frac{8}{9} \times T_{\rm SS}$, using STM assumptions from Sect. 3, the Lambertian emission model and the sub-solar temperature from Eq. (2)). This calculation yields on the average 0.982/0.986/1.011 for the blue/green/red channels, respectively, with small variation among the targets of our sample.

The absolute flux density calibration of PACS is based on standard stars and large main belt asteroids and has the uncertainties of 3%/3%/5% for the blue/green/red bands (PACS photometer – Point Source Flux Calibration 2011). We have taken these uncertainties into account in the PACS flux densities used in the modeling, although their contribution to the total uncertainty is small compared to the signal-to-noise ratio of our observations.

The color corrected flux densities are given in Table 3. They were determined from the combined maps of two visits, in total 4 AORs for the blue and green channels and 8 AORs for the red. The only exceptions are 19521 Chaos and 90568 (2004 GV_9), whose one map was excluded from our analysis due to a problem in obtaining reliable photometry from those observations. The uncertainties include the photometric 1σ and absolute calibration 1σ uncertainties. 17 targets were detected in at least one PACS channel. The upper limits are the 1σ noise levels of the maps, including both the instrumental noise and residuals from the eliminated infrared background confusion noise. 79360 Sila has a flux density which is lower by a factor of three in the red channel than the one published by Müller et al. (2010). We have re-analyzed this earlier chopped/nodded observation using the latest knowledge on calibration and data reduction and found no significant change in the flux density values. As speculated in Müller et al. (2010) the 2009 single-visit *Herschel* observation was most probably contaminated by a background source.

2.4. Complementary Spitzer observations

About 75 TNOs and Centaurs in the "TNOs are Cool" program were also observed by the *Spitzer* Space Telescope (Werner et al. 2004) using the Multiband Imaging Photometer for *Spitzer* (MIPS; Rieke et al. 2004). 43 targets were detected at a useful signal-to-noise ratio in both the 24 μm and 70 μm bands of that instrument. As was done for our *Herschel* program, many of the *Spitzer* observations utilized multiple AORs for a single target, with the visits timed to allow subtraction of background confusion. The MIPS 24 μm band, when combined with 70−160 μm data, can provide very strong constraints on the temperature of the warmest regions of a TNO.

The absolute calibration, photometric methods and color corrections for the MIPS data are described in Gordon et al. (2007), Engelbracht et al. (2007) and Stansberry et al. (2007). Nominal

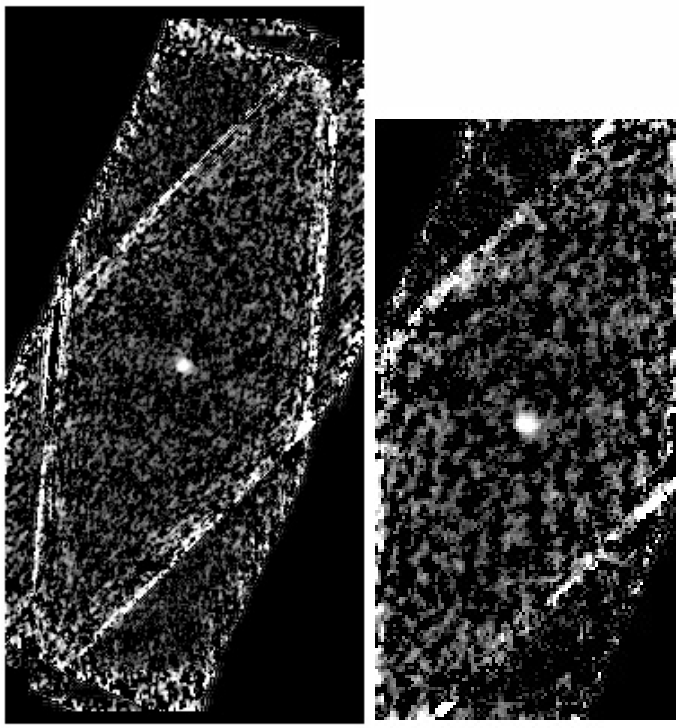

Fig. 2. Combined maps of 120347 Salacia from the individual maps (Fig. 1) in the green (left) and red channels. Orientation: north is up and east is to the left.

Table 3. Color corrected *Herschel* flux densities of the sample of 19 classical TNOs from coadded images of two visits.

Target	F_{70} (mJy)	F_{100} (mJy)	F_{160} (mJy)
119951 (2002 KX_{14})	7.4 ± 0.7	10.2 ± 1.3	7.2 ± 1.7
(2001 XR_{254})	2.5 ± 0.7	<1.0	<1.4
275809 (2001 QY_{297})	1.1 ± 1.1	4.2 ± 0.8	2.4 ± 1.1
(2001 RZ_{143})	2.2 ± 0.7	<1.1	<1.1
(2002 GV_{31})	<0.8	<1.1	<1.7
79360 Sila	3.9 ± 0.8	5.5 ± 1.1	<5.7
88611 Teharonhiawako	1.9 ± 0.7	2.1 ± 0.9	<2.1
120181 (2003 UR_{292})	<4.6	3.9 ± 1.1	<3.8
(2005 EF_{298})	1.4 ± 0.6	1.7 ± 0.8	<1.9
138537 (2000 OK_{67})	<0.9	<0.8	<3.1
148780 Altjira	3.4 ± 1.0	4.3 ± 1.6	<2.1
(2002 KW_{14})	1.9 ± 0.8	<3.0	<1.4
(2001 KA_{77})	<2.1	2.7 ± 1.0	<1.7
19521 Chaos	9.2 ± 2.2[a]	11.3 ± 1.2	10.3 ± 1.8
78799 (2002 XW_{93})	17.0 ± 0.9	17.8 ± 1.5	12.9 ± 1.9
(2002 MS_4)	26.3 ± 1.3	35.8 ± 1.5	21.6 ± 4.2
145452 (2005 RN_{43})	24.8 ± 1.3	23.9 ± 1.8	13.9 ± 1.9
90568 (2004 GV_9)	16.9 ± 1.0	19.3 ± 1.9[b]	18.3 ± 2.9
120347 Salacia	30.0 ± 1.2	37.8 ± 2.0	28.1 ± 2.7

Notes. F_{70}, F_{100} and F_{160} are the monochromatic flux densities of the PACS blue/green/red channels. [(a)] Observation 1342202317 excluded. [(b)] Observation 1342202923 excluded.

calibration uncertaintes are 2% and 4% in the 24 μm and 70 μm bands respectively. To allow for additional uncertainties that may be caused by the sky-subtraction process, application of color corrections, and the faintness of TNOs relative to the MIPS stellar calibrators, we adopt uncertainties of 3% and 6% as has been done previously for MIPS TNO data (e.g. Stansberry et al. 2008; Brucker et al. 2009). The effective monochromatic wavelengths of the two MIPS bands we use are 23.68 μm and 71.42 μm. With an aperture of 0.85 m the telescope-limited spatial resolution is 6″ and 18″ in the two bands.

Spitzer flux densities of 13 targets overlapping our classical TNO sample are given in Table 4. The new and re-analyzed flux densities are based on re-reduction of the data using updated ephemeris positions. They sometimes differ by 10″ or more from those used to point *Spitzer*. The ephemeris information is used in the reduction of the raw 70 μm data, for generating the sky background images, and for accurate placement of photometric apertures. This is especially important for the Classical TNOs which are among the faintest objects observed by *Spitzer*. Results for four targets are previously unpublished: 275809 (2001 QY_{297}), 79360 Sila, 88611 Teharonhiawako, and 19521 Chaos. As a result of the reprocessing of the data, the fluxes for 119951 (2002 KX_{14}), 148780 Altjira, 2001 KA_{77} and 2002 MS_4 differ from those published in Brucker et al. (2009) and Stansberry et al. (2008).

The 70 μm bands of PACS and MIPS are overlapping and the flux density values agree typically within ±5% for the six targets observed by both instruments with $SNR \gtrsim 2$.

2.5. Optical photometry

The averages of V-band or R-band absolute magnitude values available in the literature are given in Table 1. The most reliable way of determining them is to observe a target at multiple phase angles and over a time span enough to determine lightcurve properties, but such complete data are available only for 119951 (2002 KX_{14}) in our sample. For all other targets assumptions about the phase behavior have been made due to the lack of coverage in the range of phase angles.

The IAU (H, G) magnitude system for photometric phase curve corrections (Bowell et al. 1989), which has been adopted in some references, is known to fail in the case of many TNOs (Belskaya et al. 2008). Due to the lack of a better system we prefer linear methods as a first approximation since TNOs have steep phase curves which do not deviate from a linear one in the limited phase angle range usually available for TNO observations. The opposition surge of very small phase angles ($\alpha \lesssim 0.2°$, Belskaya et al. 2008) has not been observed for any of our 19 targets due to the lack of observations at such small phase angles. All of our *Herschel* and *Spitzer* observations are limited to the range $1.0° < \alpha < 2.1°$.

We have used the linear method ($H_V = V - 5\log(r\Delta) - \beta\alpha$, where V is the apparent V-magnitude in the Johnson-Coussins or the Bessel V-band, and other symbols are as in Table 2, and β is the linearity coefficient) to calculate the H_V values from individual V-magnitudes given in the references (see Table 5) for 2001 XR_{254}, 275809 (2001 QY_{297}), 79360 Sila, 88611 Teharonhiawako, 148780 Altjira and 19521 Chaos. In order to be consistent with most of the H_V values in the literature we have adopted $\beta = 0.14 \pm 0.03$ calculated from Sheppard & Jewitt (2002). The effect of slightly different values of β or assumptions of its composite value used in previous works is usually negligible compared to uncertainties caused by lightcurve variability (an exception is 90568 (2004 GV_9)).

For five targets with no other sources available we take the absolute magnitudes in the R-band (H_R in Table 5) from the Minor Planet Center and calculate their standard deviation, since the number of V-band observations for these targets is very low, and use the average $(V - R)$ color index for classical TNOs 0.59 ± 0.15 (Hainaut & Delsanti 2002) to derive H_V. While the MPC is mainly used for astrometry and the magnitudes are

Table 4. Complementary *Spitzer* observations.

Target	Duration (min)	Starting day of observing epoch	r	Δ	α	Previous works MIPS F_{24} (mJy)	Previous works MIPS F_{70} (mJy)	This work MIPS F_{24} (mJy)	This work MIPS F_{70} (mJy)
119951	128.10	2005-08-26	39.61	39.59	1.5	0.0786 ± 0.0082^a	2.22 ± 1.45^a	0.080 ± 0.013	7.7 ± 1.7
119951	37.27	2006-03-30	39.58	39.20	1.4	$<0.0363^b$	$<3.90^b$	0.083 ± 0.029	...
275809	594.87	2008-11-21	42.76	42.39	1.3	...	...	<0.01	<1.5
(2001 RZ_{143})	203.30	2004-12-26	41.38	40.98	1.3	0.046 ± 0.008^a	$<0.7^a$	...	...
79360	494.70	2008-05-18	43.52	43.30	1.3	...	...	0.05 ± 0.01	<2.7
88611	398.42	2004-11-04	45.00	44.67	1.2	...	...	0.029 ± 0.010	0.7 ± 0.6
138537	257.45	2004-11-04	40.57	40.11	1.3	0.031 ± 0.007^a	$<0.8^a$	...	...
148780	400.92	2006-02-16	45.33	45.08	1.2	0.0167 ± 0.0025^a	$<0.85^a$	0.020 ± 0.008	<1.67
(2002 KW_{14})	213.05	2005-08-26	40.04	40.03	1.5	$<0.006^a$	3.3 ± 1.1^a	...	...
(2001 KA_{77})	400.90	2006-03-31	48.56	48.35	1.2	0.0077 ± 0.0023^a	4.12 ± 0.81^a	<0.025	<1.4
19521	66.06	2004-09-24	42.05	41.68	1.3	...	...	...	9.0 ± 3.0
(2002 MS_4)	82.04	2006-03-31	47.39	47.48	1.2	0.391 ± 0.022^b	20.0 ± 4.1^b	0.40 ± 0.02	24.7 ± 2.9
90568	57.00	2005-01-28	38.99	39.01	1.5	0.166 ± 0.010^b	17.5 ± 2.2^b	...	...
120347	227.62	2006-12-03	43.82	43.39	1.2	0.546 ± 0.021^c	36.6 ± 3.7^c	...	...

Notes. The duration includes the total time of several visits. Observing epochs lasted 1−14 days. The other quantities are as in Table 2. Targets below the horizontal line have $i > 4.5°$. The *Spitzer* program IDs are: 55 (for the observations of Chaos), 3229 (Teharonhiawako), 3283 (2002 KX14 in 2006, 2002 MS4, 2004 GV9), 3542 (2002 KX14 in 2005, 2001 RZ143, 2000 OK67, Altjira, 2002 KW14, 2001 KA77), 30081 (Salacia), 40016 (Sila), and 50024 (2001 QY297).

References. [(a)] Color corrected MIPS flux density with 1σ measurement uncertainty from Brucker et al. (2009) together with quadratically added calibration uncertainties. [(b)] Stansberry et al. (2008), uncertainty calculated from SNR and includes quadratically added calibration uncertainties, upper limits shown here are 1-σ. [(c)] Stansberry et al. (2012).

Table 5. Overview of optical auxiliary data.

Target	H_V ref.	0°-phase method ([β] = mag/°)	L.c. Δm_R (mag)	L.c. period (h)	Corrected H_V (mag)	Corrections included
119951 (2002 KX_{14})	(a)	phase study	...	...	4.86 ± 0.10	assumed Δm_R
(2001 XR_{254})*	(b)	(1)	(>a few 0.1:s)[l]	...	6.05 ± 0.15	Δm_R
275809 (2001 QY_{297})*	(c, d, e)	(1)	0.49–0.66[c]	...	5.86 ± 0.31	Δm_R
(2001 RZ_{143})*	(f)	$\beta = 0.16^f$	...	...	6.69 ± 0.13	assumed Δm_R
(2002 GV_{31})	(g)	(2)	...	...	6.1 ± 0.6	...
79360 Sila*	(h, i, j, k)	(1)	$<0.08^u$	...	5.56 ± 0.04	Δm_R
88611 Teharonhiawako*	(l)	(1)	0.2^v	4.7526 ± 0.0007^v	6.00 ± 0.13	Δm_R
120181 (2003 UR_{292})	(g)	$\beta_R = 0.14^t$	...	...	7.4 ± 0.4	...
(2005 EF_{298})	(g)	(2)	...	...	6.4 ± 0.5	...
138537 (2000 OK_{67})	(m, n)	$\beta = 0.15^m / 0.14^n$	...	...	6.47 ± 0.13	assumed Δm_R
148780 Altjira*	(o, p, d)	(1)	$<0.3^p$	...	6.44 ± 0.14	Δm_R
(2002 KW_{14})	(q)	(1)	$0.21 / 0.26^c$	...	5.88 ± 0.11	Δm_R
(2001 KA_{77})	(o)	(1)	...	...	5.64 ± 0.12	assumed Δm_R
19521 Chaos	(h, i, n, r)	(1)	$<0.10^u$	...	5.00 ± 0.06	Δm_R
78799 (2002 XW_{93})	(g)	(2)	...	...	5.4 ± 0.7	...
(2002 MS_4)	(g)	(2)	...	...	4.0 ± 0.6	...
145452 (2005 RN_{43})	(q)	(1)	0.04 ± 0.01^p	$5.62/7.32^x$	3.89 ± 0.05	Δm_R
90568 (2004 GV_9)	(s)	$\beta = 0.18 \pm 0.06^p$	0.16 ± 0.03^w	5.86 ± 0.03^w	4.23 ± 0.10	β, Δm_R
120347 Salacia*	(q)	(1)	0.03 ± 0.01^x	$6.09/8.1^x$	4.24 ± 0.04	Δm_R

Notes. The average absolute V-band (or R-band) magnitudes from literature are given in Table 1, and this table gives the absolute V-magnitudes with uncertainties which take into account the lightcurve (L.c.) amplitude Δm_R (either in the *UBVRI* system R-band or Sloan's r'-band). The 0°-phase method (see text) tells how the extrapolation to zero phase was done (either in the reference or in this work). The last column indicates which corrections are significant in contributing to the corrected H_V. * Denotes a known binary system (Noll et al. 2008). (1) V-band linear phase coefficient $\beta = 0.14 \pm 0.03$ (Sheppard & Jewitt 2002, β calculated from values therein). (2) R-band linear phase coefficient $\beta_R = 0.12$ (Average from Belskaya et al. 2008).

References. [(a)] Rabinowitz et al. (2007). [(b)] Grundy et al. (2009). [(c)] Thirouin et al. (2012). [(d)] Grundy et al. (2011). [(e)] Doressoundiram et al. (2007). [(f)] Santos-Sanz et al. (2009). [(g)] IAU Minor Planet Center/List of Transneptunian Objects at URL `http://www.minorplanetcenter.net/iau/lists/TNOs.html` accessed June 2011. [(h)] Boehnhardt et al. (2001). [(i)] Davies et al. (2000). [(j)] Barucci et al. (2000). [(k)] Grundy et al. (2012). [(l)] Benecchi et al. (2009). [(m)] Benecchi et al. (2011). [(n)] Doressoundiram et al. (2002). [(o)] Doressoundiram et al. (2005). [(p)] Sheppard (2007). [(q)] Perna et al. (in prep.). [(r)] Tegler & Romanishin (2000). [(s)] DeMeo et al. (2009). [(t)] Calculated from MPC data from 16 observations. [(u)] Sheppard & Jewitt (2002). [(v)] Osip et al. (2003), lightcurve caused by secondary component, amplitude calculated for the combined system. [(w)] Dotto et al. (2008). [(x)] Thirouin et al. (2010).

considered to be inaccurate by some works (e.g. Benecchi et al. 2011; Romanishin & Tegler 2005), for the five targets we use the average of 9 to 16 R-band observations and adopt the average R-band phase coefficient $\beta_R = 0.12$ (calculated from Belskaya et al. 2008).

The absolute V-magnitudes used as input in our analysis (the "Corrected H_V" column in Table 5) take into account additional uncertainties from known or assumed variability in H_V. The amplitude, the period and the time of zero phase of the lightcurves of three hot classicals (145452 (2005 RN_{43}), 90568 (2004 GV_9) and 120347 Salacia) are available in the literature, but even for these three targets the uncertainty in the lightcurve period is too large to be used for exact phasing with *Herschel* observations. The lightcurve amplitude or amplitude limit is known for half of our targets and for them we add 88% of the half of the peak-to-peak amplitude (1σ i.e. 68% of the values of a sinusoid are within this range) quadratically to the uncertainty of H_V. According to a study of a sample of 74 TNOs from various dynamical classes (Duffard et al. 2009) 70% of TNOs have a peak-to-peak amplitude $\lesssim$0.2 mag, thus we quadratically add 0.09 mag to the uncertainty of H_V for those targets in our sample for which lightcurve information is not available.

3. Thermal modeling

The combination of observations from thermal-infrared and optical wavelengths allows us to estimate various physical properties via thermal modeling. For a given temperature distribution the disk-integrated thermal emission F observed at wavelength λ is

$$F(\lambda) = \frac{\epsilon(\lambda)}{\Delta^2} \int_S B(\lambda, T(S))\ \mathrm{d}\boldsymbol{S} \cdot \boldsymbol{u}, \tag{1}$$

where ϵ is the emissivity, Δ the observer-target distance, $B(\lambda, T)$ Planck's radiation law for black bodies, $T(S)$ the temperature distribution on the surface S and $\boldsymbol{u}$ the unit directional vector toward the observer from the surface element $\mathrm{d}\boldsymbol{S}$. The temperature distribution of an airless body depends on physical parameters such as diameter, albedo, thermal inertia, and surface roughness.

There are three basic types of models to predict the emission of an asteroid with a given size and albedo assuming an equilibrium between insolation and re-emitted thermal radiation: the Standard Thermal Model (STM), the Fast-rotating Isothermal Latitude thermal model (Veeder et al. 1989), and the thermophysical models (starting from Matson 1971; e.g. Spencer et al. 1989; Lagerros 1996). While originally developed for asteroids in the mid-IR wavelengths these models are applicable for TNOs, whose thermal peak is in the far-IR.

The STM (cf. Lebofsky et al. 1986, and references therein) assumes a smooth, spherical asteroid, which is not rotating and/or has zero thermal inertia, and is observed at zero phase angle. The subsolar temperature T_{SS} is

$$T_{\mathrm{SS}} = \left[\frac{(1-A)\,S_\odot}{\epsilon\eta\sigma r^2}\right]^{\frac{1}{4}}, \tag{2}$$

where A is the Bond albedo, $S_\odot$ is the solar constant, η is the beaming factor, σ is the Stefan-Boltzmann constant and r is the heliocentric distance. In the STM ϵ does not depend on wavelength. The beaming factor η adjusts the subsolar temperature. The canonical value $\eta = 0.756$ is based on calibrations using the largest few main belt asteroids. The STM assumes an average linear infrared phase coefficient of 0.01 mag/degree based on observations of main belt asteroids.

In this work we use the Near-Earth Asteroid Thermal Model NEATM (Harris 1998). The difference to the STM is that in the NEATM η is fitted with the data instead of using a single canonical value. For rough surfaces η takes into account the fact that points on the surface S radiate their heat preferentially in the sunward direction. High values ($\eta > 1$) lead to a reduction of the model surface temperature, mimicking the effect of high thermal inertia, whereas lower values are a result of surface roughness. Furthermore, the phase angle α is taken into account by calculating the thermal flux an observer would detect from the illuminated part of S assuming a Lambertian emission model and no emission from the non-illuminated side.

Whenever data quality permits we treat η as a free fitting parameter. However, in some cases of poor data quality this method leads to η values which are too high or too low and therefore unphysical. In these cases we fix it to a canonical value of $\eta = 1.20 \pm 0.35$ derived by Stansberry et al. (2008) from *Spitzer* observations of TNOs. The physical range of η values is determined by using NEATM as explained in Mommert et al. (2012) to be $0.6 \leq \eta \leq 2.6$.

Throughout this work we assume the surface emissivity $\epsilon = 0.9$, which is based on laboratory measurements of silicate powder up to a wavelength of 22 μm (Hovis & Callahan 1966) and a usual approximation for small bodies in the solar system. At far-IR wavelengths the emissivity of asteroids may be decreasing as a function of wavelength (Müller & Lagerros 1998) from 24 to 160 μm, but the amount depends on individual target properties. Thus, a constant value is assumed for simplicity. The variation of emissivity of icy surfaces as a function of wavelength could in principle provide hints about surface composition. H_2O ice has an emissivity close to one with small variations (Schmitt et al. 1998) whereas other ices may show a stronger wavelength dependence (e.g. Stansberry et al. 1996). Near-IR spectroscopic surface studies have been done for five of our targets but none of them show a reliable detection of ices, even though many dynamically hot classicals are known to have ice signatures in their spectra (Barucci et al. 2011).

For the Bond albedo we assume that $A \approx A_V$ since the V-band is close to the peak of the solar spectrum. The underlying assumption is that the Bond albedo is not strongly varying across the relevant solar spectral range of reflected light. The Bond albedo is connected to the geometric albedo via $A_V = p_V q$, where q is the phase integral and p_V the geometric albedo in V-band. Instead of the canonical value of $q = 0.39$ (Bowell et al. 1989) we have adopted $q = 0.336 p_V + 0.479$ (Brucker et al. 2009), which they used for a *Spitzer* study of classical TNOs. From the definition of the absolute magnitude of asteroids we have:

$$p_V S_{\mathrm{proj}} = \pi a^2 \times 10^{\frac{2}{5}(m_\odot - H_V)}, \tag{3}$$

where S_{proj} is the area projected toward the observer, a is the distance of one astronomical unit, $m_\odot$ is the apparent V-magnitude of the Sun, and H_V is the absolute V-magnitude of the asteroid. We use $m_\odot = (-26.76 \pm 0.02)$ mag (Bessell et al. 1998; Hayes 1985). An error of 0.02 mag in H_V means a relative error of 1.8% in the product (3).

We find the free parameters p_V, $D = \sqrt{\frac{4S_{\mathrm{proj}}}{\pi}}$ and η in a weighted least-squares sense by minimizing the cost function

$$\chi^2_\nu = \frac{1}{\nu} \sum_{i=1}^{N} \frac{[F(\lambda_i) - F_{\mathrm{model}}(\lambda_i)]^2}{\sigma_i^2}, \tag{4}$$

where ν is the number of degrees of freedom, N is the number of data points in the far-infrared wavelengths, $F(\lambda_i)$ is the observed

flux density at wavelength λ_i with uncertainty σ_i, and $F_{\rm model}$ is the modeled emission spectrum. When only upper flux density limits are available, they are treated as having zero flux density with a 1σ uncertainty equal to the upper limit flux density uncertainty ($0 \pm \sigma$). The cost function (4) does not follow the χ^2 statistical distribution since in a non-linear fit the residuals are not normally distributed even if the flux densities had normally distributed uncertainties.

3.1. Error estimates

The error estimates of the geometric albedo, the diameter and the beaming parameter are determined by a Monte Carlo method described in Mueller et al. (2011). We generate 500 sets of synthetic flux densities normally distributed around the observed flux densities with the same standard deviations as the observations. Similarly, a set of normally distributed H_V values is generated. For those targets whose $\chi^2 \gg 1$ we do a rescaling of the errorbars of the flux densities before applying the Monte Carlo error estimation as described in Santos-Sanz et al. (2012) and illustrated in Mommert et al. (2012).

The NEATM model gives us the effective diameter of a spherical target. 70−80% of TNOs are known to be MacLaurin spheroids with an axial ratio of 1.15 (Duffard et al. 2009; Thirouin et al. 2010). When the projected surface has the shape of an ellipse instead of a circle, then this ellipse will emit more flux than the corresponding circular disk which has the same surface because the Sun is seen at higher elevations from a larger portion of the ellipsoid than on the sphere. Therefore, the NEATM diameters may be slightly overestimated. Based on studies of model accuracy (e.g. Harris 2006) we adopt uncertainties of 5% in the diameter estimates and 10% in the p_V estimates to account for systematic model errors when NEATM is applied at small phase angles.

4. Results of individual targets

In this Section we give the results of model fits using the NEATM to determine the area-equivalent diameters (see Sect. 3) as well as geometric albedos and beaming factors. We note that our observations did not spatially resolve binary systems, we therefore find area-equivalent diameters of the entire system rather than component diameters; this will be further discussed in Sect. 5.2.

In cases where also *Spitzer*/MIPS data are available for a target we determine the free parameters for both PACS only and the combined data sets. The solutions are given in Table 6. A floating-η solution is only adopted if its χ^2 is not much greater than unity. The exact limit depends on the number of data points. For $N = 5$ this limit is $\chi^2 \lesssim 1.7$. For the PACS-only data set we may adopt floating-η solutions only if there are no upper-limit data points. 138537 (2000 OK_{67}) has only upper limits from PACS, therefore only the solution using combined data is shown. 2001 RZ_{143} has five data points, three of which are upper limits. The PACS flux density at 70 μm is approximately a factor of three higher than the MIPS upper limit (see Tables 3 and 4). For this target we adopt the model solution determined without the MIPS 70 μm channel. The best solution for each target is shown in Fig. 3.

The radiometric diameters determined with data from the two instruments are on the average close to the corresponding results using PACS data alone, but there are some significant differences as well, most notably 275809 (2001 QY_{297}) and 2002 KW_{14}. The former has a PACS-only solution, which is within the error bars of the green and red channel data points, but above the PACS blue channel data point. When the two upper limits from MIPS are added in the analysis the model solution is at a lower flux level below the PACS green channel data point but compatible with the other data (see Fig. 3). 2002 KW_{14} has upper limits in the PACS green and red channels as well as in the MIPS 24 μm channel. Without this upper limit in the shortest wavelength the PACS-only solution is at higher flux levels in short wavelengths and gives a lower flux at long wavelengths.

When choosing the preferred solution we are comparing two fits with different numbers of data points used, therefore in this comparison we calculate χ^2 for the PACS-only solution using the same data points as for the combined solution taking into account the different observing geometries during *Herschel* and *Spitzer* observations. In all cases where MIPS data is available the solution based on the combined data from the two instruments is the preferred one.

2002 GV_{31} is the only non-detection by both PACS and MIPS in our sample of 19 targets. The astrometric 3σ uncertainty at the time of the PACS observation was <4″ (semimajor axis of the confidence ellipsoid[2]), which is well within the high-coverage area of our maps.

The error bars from the Monte Carlo error estimation method may sometimes be too optimistic compared to the accuracy of optical data and the model uncertainty of NEATM (see Sect. 3). We check that the uncertainty of geometric albedo is not better than the uncertainty implied by the optical constraint (Eq. (3)) due to uncertainties in H_V and $m_\odot$. The lower p_V uncertainty of four targets is limited by this (see Table 6).

5. Discussion

Our new size and geometric albedo estimates improve the accuracy of previous estimates of almost all the targets with existing results or limits (Table 7). Two thirds of our targets have higher albedos (Table 6) than the 0.08 used in the planning of these observations, which has lead to the lower than expected SNRs and several upper limit flux densities (Table 3). Previous results from *Spitzer* are generally compatible with our new estimates. However, two targets are significantly different: 119951 (2002 KX_{14}) and 2001 KA_{77}, whose solutions are compatible with the optical constraint (Eq. (3)), but the new estimate has a large diameter and low albedo (target 119951) instead of a small diameter and high albedo, or vice versa (target 2001 KA_{77}). It can be noted that there is a significant difference in the reprocessed *Spitzer* flux densities at 70 μm compared to the previously published values (see Table 4), which together with the PACS 100 μm data can explain the significant change in the diameter and geometric albedo estimates. Our new estimates for 148780 Altjira differ from the previous upper and lower limits based on *Spitzer* data alone (Table 7). This change can be explained by the addition of the 70 μm and 100 μm PACS data points (Table 3) to the earlier MIPS 24 μm value and the MIPS 70 μm upper flux density limit (Table 4).

The diameter estimates in our sample are ranging from 100 km of 120181 (2003 UR_{292}) up to 930 km of 2002 MS_4, which is larger than previously estimated for it. 2002 MS_4 and 120347 Salacia are among the ten largest TNOs with sizes similar to those of 50000 Quaoar and 90482 Orcus. The

[2] Asteroids Dynamic Site by A. Milani, Z. Knezevic, O. Arratia et al., URL: http://hamilton.dm.unipi.it/astdys/, accessed August 2011, calculations based on the OrbFit software.

Table 6. Solutions for radiometric diameters and geometric albedos (see text for explanations).

Target	Instruments	D (km)	Binary?	p_V[a]	η
119951 (2002 KX_{14})	PACS	485^{+83}_{-93}	no	$0.086^{+0.042}_{-0.023}$	$2.07^{+0.88}_{-0.82}$
	PACS, MIPS	455 ± 27		$0.097^{+0.014}_{-0.013}$	$1.79^{+0.16}_{-0.15}$
(2001 XR_{254})	PACS	200^{+49}_{-63}	yes	$0.17^{+0.19}_{-0.05}$	1.2 ± 0.35 (fixed)
275809 (2001 QY_{297})	PACS	278^{+45}_{-55}	yes	$0.104^{+0.094}_{-0.050}$	1.2 ± 0.35 (fixed)
	PACS, MIPS	200^{+62}_{-59}		$0.20^{+0.25}_{-0.11}$	1.2 ± 0.35 (fixed)
(2001 RZ_{143})	PACS	168^{+47}_{-52}	yes	$0.13^{+0.15}_{-0.05}$	1.2 ± 0.35 (fixed)
	PACS, MIPS[b]	140^{+39}_{-33}		$0.191^{+0.066}_{-0.045}$	$0.75^{+0.23}_{-0.19}$
(2002 GV_{31})	PACS	<130	no	>0.22	1.2 ± 0.35 (fixed)
79360 Sila	PACS	333^{+38}_{-47}	yes	$0.095^{+0.033}_{-0.020}$	1.2 ± 0.35 (fixed)
	PACS, MIPS	343 ± 42		$0.090^{+0.027}_{-0.017}$	$1.36^{+0.21}_{-0.19}$
88611 Teharonhiawako	PACS	234^{+37}_{-39}	yes	$0.129^{+0.062}_{-0.036}$	1.2 ± 0.35 (fixed)
	PACS, MIPS	177^{+46}_{-44}		$0.22^{+0.14}_{-0.08}$	$0.86^{+0.37}_{-0.29}$
120181 (2003 UR_{292})	PACS	104^{+22}_{-24}	no	$0.16^{+0.19}_{-0.08}$	1.2 ± 0.35 (fixed)
(2005 EF_{298})	PACS	174^{+27}_{-32}	no	$0.16^{+0.13}_{-0.07}$	1.2 ± 0.35 (fixed)
138537 (2000 OK_{67})	PACS, MIPS	151^{+31}_{-37}	no	$0.20^{+0.21}_{-0.08}$	1.2 ± 0.35 (fixed)
148780 Altjira	PACS	313^{+50}_{-48}	yes	$0.048^{+0.022}_{-0.015}$	1.2 ± 0.35 (fixed)
	PACS, MIPS	257^{+90}_{-92}		$0.071^{+0.049}_{-0.021}$	1.46 ± 0.41
(2002 KW_{14})	PACS	181^{+36}_{-38}	no	$0.24^{+0.14}_{-0.07}$	1.2 ± 0.35 (fixed)
	PACS, MIPS	319^{+74}_{-81}		$0.08^{+0.14}_{-0.05}$	$2.50^{+0.14}_{-1.64}$
(2001 KA_{77})	PACS	252^{+49}_{-57}	no	$0.155^{+0.091}_{-0.046}$	1.2 ± 0.35 (fixed)
	PACS, MIPS	310^{+170}_{-60}		$0.099^{+0.052}_{-0.056}$	$2.52^{+0.18}_{-0.83}$
19521 Chaos	PACS	600^{+140}_{-150}	no	$0.050^{+0.040}_{-0.019}$	$2.2^{+1.6}_{-1.0}$
	PACS, MIPS	600^{+140}_{-130}		$0.050^{+0.030}_{-0.016}$	$2.2^{+1.2}_{-1.1}$
78799 (2002 XW_{93})	PACS	565^{+71}_{-73}	no	$0.038^{+0.043}_{-0.025}$	$0.79^{+0.27}_{-0.24}$
(2002 MS_4)	PACS	988^{+96}_{-105}	no	$0.046^{+0.042}_{-0.026}$	1.2 ± 0.35 (fixed)
	PACS, MIPS	934 ± 47[c]		$0.051^{+0.036}_{-0.022}$	1.06 ± 0.06
145452 (2005 RN_{43})	PACS	679^{+55}_{-73}	no	$0.107^{+0.029}_{-0.018}$	1.2 ± 0.35 (fixed)
90568 (2004 GV_9)	PACS	670^{+210}_{-180}	no	$0.08^{+0.15}_{-0.06}$	$1.9^{+1.5}_{-0.8}$
	PACS, MIPS	680 ± 34[c]		$0.0770^{+0.0084}_{-0.0077}$	$1.93^{+0.09}_{-0.07}$
120347 Salacia	PACS	994^{+88}_{-74}	yes	$0.0361^{+0.0059}_{-0.0055}$	$1.47^{+0.29}_{-0.25}$
	PACS, MIPS	901 ± 45[c]		0.0439 ± 0.0044[d]	1.156 ± 0.031

Notes. For binary systems D is the area-equivalent system diameter. In case of two solutions the preferred one is based on data from both PACS and MIPS instruments. [(a)] Lower uncertainty limited by the uncertainty of H_V for 275809/PACS-MIPS, 2005 EF_{298}, 78799, and 2002 MS_4/both solutions. [(b)] MIPS 70 μm channel excluded. [(c)] Error estimate limited by the adopted diameter uncertainty of 5% of the NEATM model. [(d)] Error estimate limited by the adopted p_V uncertainty of 10% of the NEATM model.

size distribution of hot classicals in our sample is wider than that of the cold classicals, which are limited to diameters of 100−350 km (Fig. 4). The diameters of eight hot classicals from literature data (Table 7) are within the same size range as the hot classicals in our sample. The cumulative size distribution of this extended set of 20 hot classicals (Fig. 5) shows two regimes of a power law distribution with a turning point between 500 and 700 km. The slope of the cumulative distribution $N(>D) \propto D^{-q}$ is $q \approx 1.4$ for the $100 < D < 600$ km ($N = 11$) objects. There are not enough targets for a reliable slope determination in the $D > 600$ km regime. The size distribution is an important property in understanding the processes of planet formation. Several works have derived it from the LF using simplifying assumptions about common albedo and distance. Fraser et al. (2010) reported a slope of the differential size distribution of 2.8 ± 1.0 for a dynamically hot TNO population (38 AU < heliocentric distance < 55 AU and $i > 5°$). Our $q + 1$ based on a small sample of measured diameters of intermediate-size hot

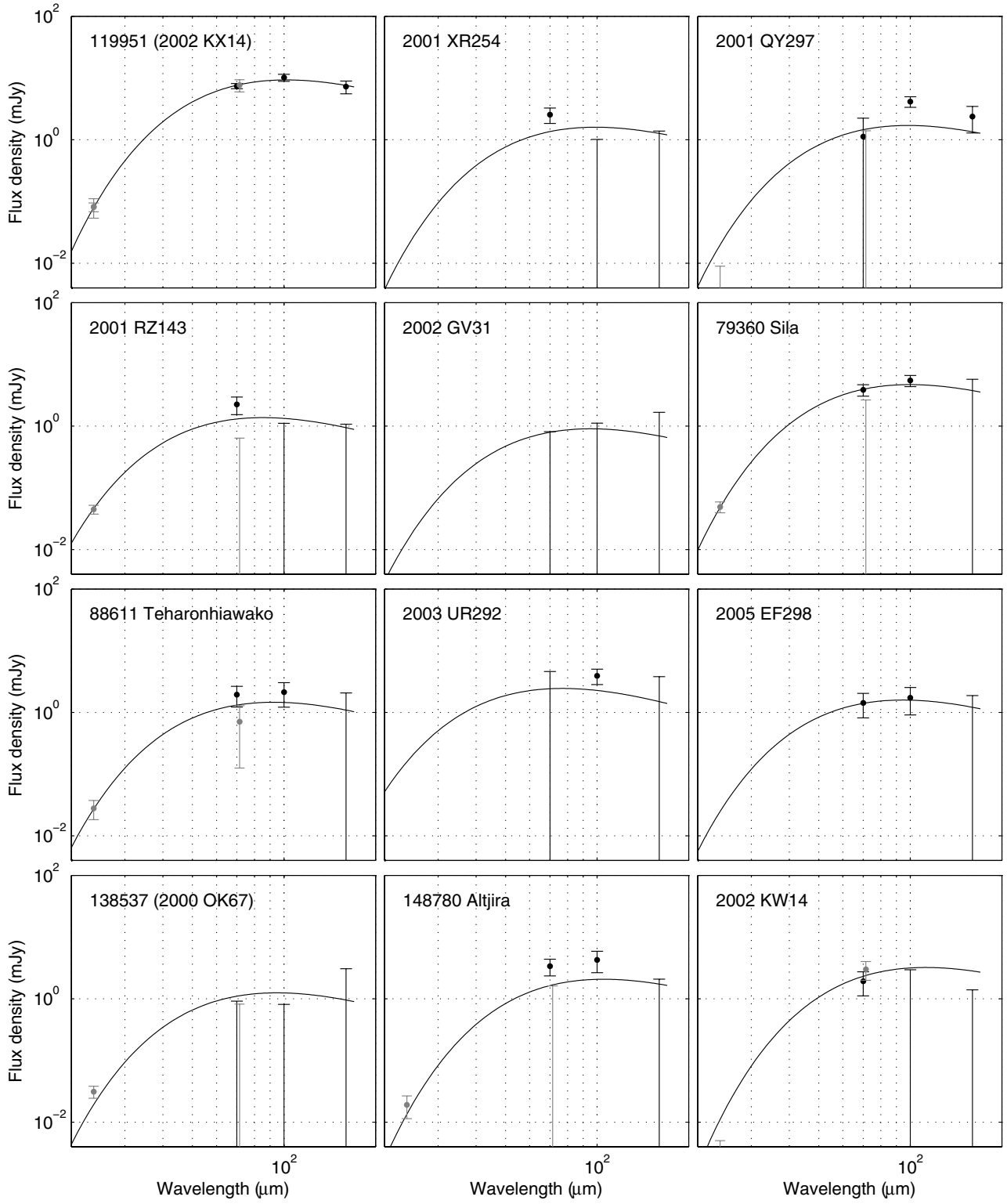

Fig. 3. Adopted model solutions from Table 6. The black data points are from PACS (70, 100 and 160 μm) and the gray points are from MIPS (24 and 71 μm) normalized to the geometry of *Herschel* observations by calculating the NEATM solution (for given D, p_V and η) at both the epochs of the *Herschel* and *Spitzer* observations and using their ratio as a correction factor.

classicals is compatible with this literature value. The high-q tail at $D > 650$ km in Fig. 5 indicates a change of slope when the population transitions from a primordial one to a collisionally relaxed population. Based on LF estimates, this change in slope for the whole TNO population was expected at 200−300 km (Kenyon et al. 2008; based on data from Bernstein et al. 2004) or at somewhat larger diameters (Petit et al. 2006). For Plutinos a change to a steeper slope occurs at 450 km (Mommert et al. 2012).

The dynamically cold and hot sub-populations are showing different geometric albedo distributions (Fig. 6) with the dynamically cold objects having higher geometric albedos in a narrower distribution. The average geometric albedo of the six cold classicals is 0.17 ± 0.04 (un-weighted average and standard

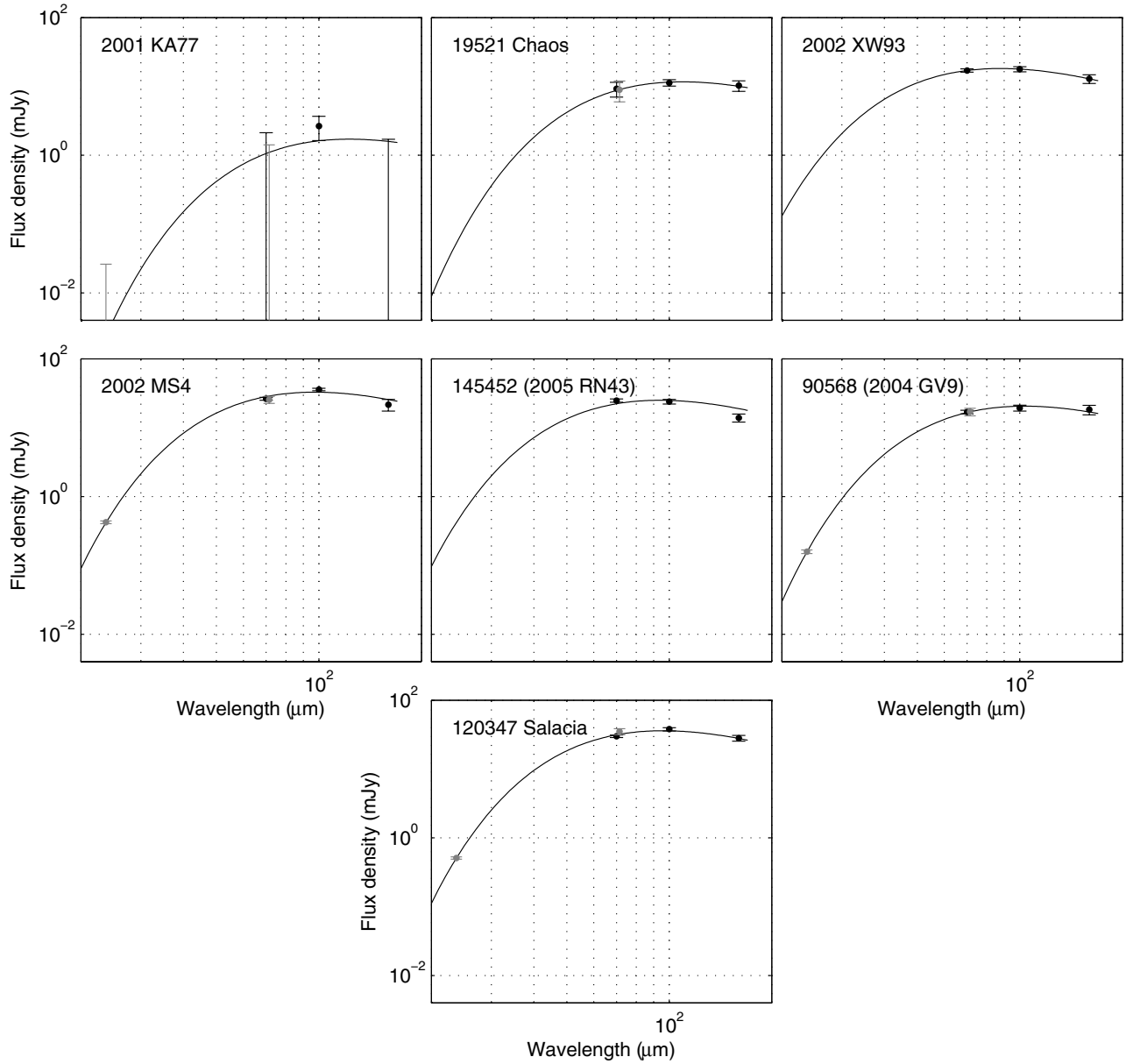

Fig. 3. continued.

deviation). The highest-albedo object is 88611 Teharonhiawako with $p_V = 0.22$, or possibly 2002 GV_{31} with the lower limit of 0.22. These findings are compatible with the conclusions of Brucker et al. (2009) based on *Spitzer* data that cold classicals have a high albedo, although we do not confirm their extreme geometric albedo of 0.6 for 119951 (2002 KX_{14}).

The darkest object in our sample is the dynamically hot target 78799 (2002 XW_{93}) with a geometric albedo of 0.038. The highest-albedo hot classicals are found in the low-i part of the sub-sample (see Fig. 7): 138537 (2000 OK_{67}) at $i = 4.9°$ has $p_V = 0.20$ and the inner belt target 120181 (2003 UR_{292}) has a geometric albedo of 0.16. The 12 hot classicals in our sample have, on the average, lower albedos than the cold ones: $p_V = 0.09 \pm 0.05$. The average of the combined hot classical sub-population of this work and literature is 0.11 ± 0.04 if 55636 (2002 TX_{300}) is excluded.

From the floating-η solutions of eight targets with data from both instruments included in the fitted solution (see Table 6 and Sect. 4) we have the average $\eta = 1.47 \pm 0.43$ (un-weighted). Most of these eight targets have $\eta > 1$ implying a noticeable amount of surface thermal inertia. It should be noted, though, that inferences about surface roughness and thermal conductivity would require more accurate knowledge of the spin axis orientation and spin period of these targets. Our average η is consistent with our default value of 1.20 ± 0.35 for fixed η fits. For comparison with other dynamical classes, the average beaming parameter of seven Plutinos is $\eta = 1.11^{+0.18}_{-0.19}$ (Mommert et al. 2012) and of seven scattered and detached objects $\eta = 1.14 \pm 0.15$ (Santos-Sanz et al. 2012). The difference of using a fixed-$\eta = 1.47$ instead of fixed-$\eta = 1.20$ is that diameters would increase, on the average, by 10% and geometric albedos decrease by 16%. These changes are within the average relative uncertainties (19% in diameter and 57% in geometric albedo) of the fixed-η solutions.

5.1. Correlations

We ran a Spearman rank correlation test (Spearman 1904) to look for possible correlations between the geometric albedo p_V,

Table 7. Adopted physical properties in comparison with previous works.

		This work		Previous work			
Target		D (km)	p_V	$\lambda_{\rm detect}$ (μm)	D (km)	p_V	Reference
119951 (2002 KX_{14})		455 ± 27	$0.097^{+0.014}_{-0.013}$	24, 71	180^{+50}_{-38}	$0.60^{+0.36}_{-0.23}$	Brucker et al. (2009)
(2001 XR_{254})	B	200^{+49}_{-63}	$0.17^{+0.19}_{-0.05}$	(binary)	130–208[a]	0.09–0.23	Grundy et al. (2011)
275809 (2001 QY_{297})	B	200^{+62}_{-59}	$0.20^{+0.25}_{-0.11}$	(binary)	128–200[a]	0.13–0.32	Grundy et al. (2011)
(2001 RZ_{143})	B	140^{+39}_{-33}	$0.191^{+0.066}_{-0.045}$	24	<160	>0.23	Brucker et al. (2009)
79360 Sila	B	343 ± 42	$0.090^{+0.027}_{-0.017}$	70, 160	250–420	0.06–0.14	Müller et al. (2010)
88611 Teharonhiawako	B	177^{+46}_{-44}	$0.22^{+0.14}_{-0.08}$	(binary)	114–180[a]	0.13–0.32	Grundy et al. (2011)
138537 (2000 OK_{67})		151^{+31}_{-37}	$0.20^{+0.21}_{-0.08}$	24	<160	>0.16	Brucker et al. (2009)
148780 Altjira	B	257^{+90}_{-92}	$0.071^{+0.049}_{-0.021}$	24	<200	>0.10	Brucker et al. (2009)
				(binary)	128–200[a]	0.06–0.14	Grundy et al. (2011)
(2002 KW_{14})		319^{+74}_{-81}	$0.08^{+0.14}_{-0.05}$	71	<360	>0.05	Brucker et al. (2009)
(2001 KA_{77})		310^{+170}_{-60}	$0.099^{+0.052}_{-0.056}$	24, 71	634^{+134}_{-92}	$0.025^{+0.010}_{-0.008}$	Brucker et al. (2009)
19521 Chaos		600^{+140}_{-130}	$0.050^{+0.030}_{-0.016}$	1200	<742	>0.033	Altenhoff et al. (2004)
(2002 MS_4)		934 ± 47	$0.051^{+0.036}_{-0.022}$	24, 71	730 ± 120	$0.073^{+0.06}_{-0.03}$	Brucker et al. (2009)
90568 (2004 GV_9)		680 ± 34	$0.0770^{+0.0084}_{-0.0077}$	24, 71	684^{+68}_{-74}	$0.073^{+0.05}_{-0.03}$	Brucker et al. (2009)
120347 Salacia	B	901 ± 45	0.0439 ± 0.0044	(binary)	720–1140[a]	0.01–0.03	Grundy et al. (2011)
				24, 71	954 ± 80	$0.0357^{+0.0072}_{-0.0056}$	Stansberry et al. (2012)
(2001 QD_{298})		...		24, 71	150^{+50}_{-40}	$0.18^{+0.17}_{-0.08}$	Brucker et al. (2009)
(1996 TS_{66})		...		24, 71	190^{+50}_{-40}	$0.12^{+0.07}_{-0.05}$	Brucker et al. (2009)
50000 Quaoar	B	...		24, 71, (direct)	890 ± 70[a]	0.18 ± 0.04	Fraser & Brown (2010)
(2002 GJ_{32})		...		24, 71	220^{+90}_{-70}	$0.12^{+0.14}_{-0.06}$	Brucker et al. (2009)
20000 Varuna		...		71	710^{+180}_{-130}	$0.09^{+0.04}_{-0.03}$	Brucker et al. (2009)
55637 (2002 UX_{25})	B	...		24, 71	680^{+120}_{-110}	$0.12^{+0.05}_{-0.03}$	Stansberry et al. (2008)
55636 (2002 TX_{300})		...		(occultation)	286 ± 10	$0.88^{+0.15}_{-0.06}$	Elliot et al. (2010)
55565 (2002 AW_{197})		...		24, 71	740 ± 100	$0.12^{+0.04}_{-0.03}$	Brucker et al. (2009)

Notes. Binary systems are indicated by "B". Column $\lambda_{\rm detect}$ lists the wavelengths used in the reference for radiometric diameters. If no radiometric result is available then binary system mass is used to give the diameter of the primary component assuming equal albedos. The second part of this table lists all other classical TNOs with radiometric or other reliable size estimates. The size of 50000 Quaoar is derived from both *Spitzer* and from direct imaging by *Hubble*. All targets in the lower part are dynamically hot. [(a)] Diameter of the primary component.

diameter D, orbital elements (inclination i, eccentricity e, semi-major axis a, perihelion distance q), beaming parameter η, visible spectral slope, as well as $B-V$, $V-R$ and $V-I$ colors[3]. The Spearman correlation is a distribution-free test less sensitive to outliers than some other more common methods (e.g. Pearson correlation). We use a modified form of the test, which takes into account asymmetric error bars and corrects the significance for small numbers statistics. The details of our method are described in Peixinho et al. (2004) and Santos-Sanz et al. (2012). The significance P of a correlation is the probability of getting a higher or equal correlation coefficient value $-1 \leq \rho \leq 1$ if no correlation existed on the parent population, from which we extracted the sample. Therefore, the smaller the P the more unlikely would be to observe a $\rho \neq 0$ if it was indeed equal to zero, i.e. the greater the confidence on the presence of a correlation is. The 99.7% confidence interval (3σ), or better, corresponds to $P = 0.003$, or smaller. We consider a "strong correlation" to have $|\rho| \geq 0.6$, and a "moderate correlation" to have $0.3 \leq |\rho| < 0.6$. Selected results from our correlation analysis are presented in Table 8 and discussed in the following subsections.

5.1.1. Correlations with diameter

We detect a strong size-inclination correlation in our target sample (see Fig. 7 and Table 8). When literature targets, all of whom are dynamically hot, are included in the analysis we get a correlation of similar strength. Previously this presumable trend has been extrapolated from the correlation between intrinsic brightness and inclination (Levison & Stern 2001). We see this strong size-inclination correlation also among the hot classicals sub-sample, but not among our cold classicals where we are limited by the small sample size.

Other orbital parameters do not correlate with size. We find no correlation between size and colors, or spectral slopes, nor between size and the beaming parameter η. The possible correlation between size and geometric albedo is discussed in Sect. 5.1.2.

5.1.2. Correlations with geometric albedo

We find evidence for an anti-correlation between diameter and geometric albedo, both in our sample and when combined with other published data of classical TNOs (see Fig. 8 and Table 8). Other dynamical populations with accurately measured diameters/albedos show a different behavior: there is no such correlation seen among the Plutinos (Mommert et al. 2012) and a combined sample of 15 scattered-disc and detached objects show a positive correlation between diameter and geometric albedo at 2.9σ level (Santos-Sanz et al. 2012).

As it might be suggested visually by the distribution of diameters of classical TNOs (see Figs. 4 and 8), we have analyzed the possibility of having two groups with different size-albedo behaviors, separating in size at $D \approx 500$ km regardless of their dynamical cold/hot membership. We have found no statistical evidence for it.

With our method of accounting for error bars, which tend to "degrade" the correlation values, geometric albedo does not correlate with H_V, orbital parameters, spectral slopes, colors, nor

[3] From the Minor Bodies in the Outer solar system data base, URL: http://www.eso.org/~ohainaut/MBOSS, accessed Nov. 2011.

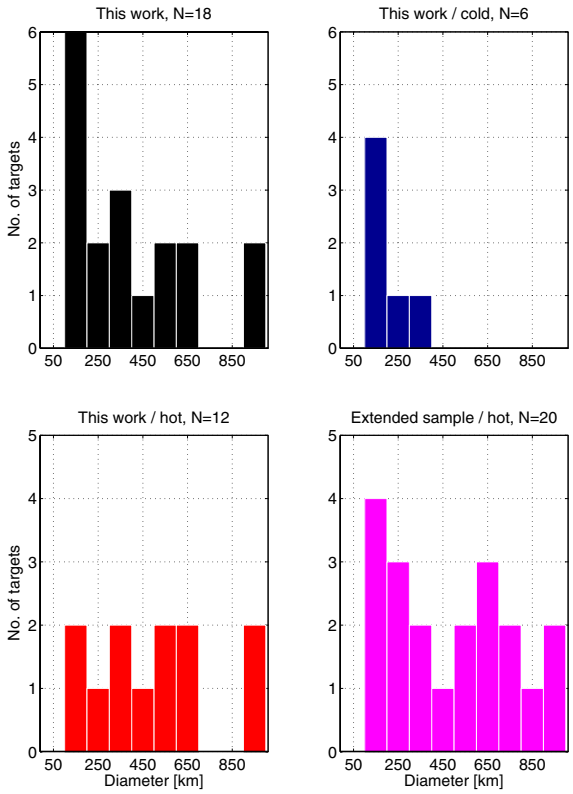

Fig. 4. Distribution of diameters from this work (*upper left*), the cold classicals of this work (*upper right*), the hot classicals of this work (*lower left*), and all hot classicals including literature results from Table 7 (*lower right*). The last plot includes only dynamically hot classicals. The bin size is 100 km.

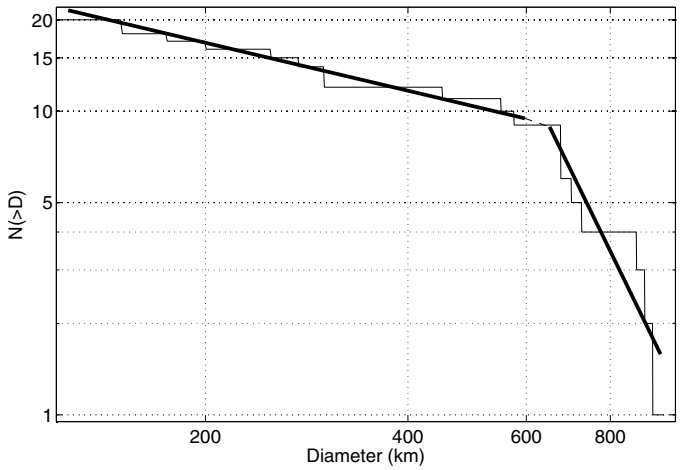

Fig. 5. Cumulative size distribution of dynamically hot classicals from this work and literature (Table 7). The power law has a change between 500 and 700 km. The intermediate size classicals have a slope parameter of $q = 1.4$.

beaming parameters η. Also when the literature targets are added we find no evidence of correlations.

5.1.3. Other correlations

The known correlations between surface color/spectral slope and orbital inclination (Trujillo & Brown 2002; Hainaut & Delsanti 2002), and between intrinsic brightness and inclination

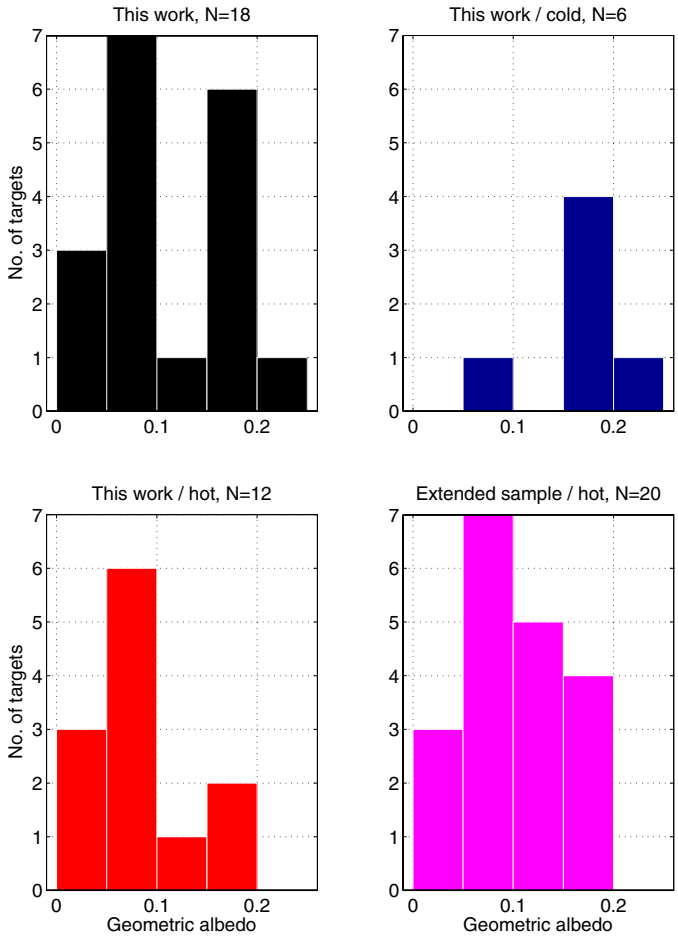

Fig. 6. Distribution of geometric albedos from this work (*upper left*), the cold classicals of this work (*upper right*), the hot classicals of this work (*lower left*), and all hot classicals including literature results from Table 7 (*lower right*). The bin size is 0.05. The Haumea family member 55636 (2002 TX_{300}) with $p_V = 0.88$ is beyond the horizontal scale.

(Levison & Stern 2001), usually interpreted as a size-inclination correlation, might lead us to conclude there was a consequent color/slope-size correlation. Our analysis with measured diameters does not show a correlation neither with spectral slope nor visible colors, as one might expect. Note, however, that we do not possess information on the surface colors/slopes of ~1/2 of our targets (~1/3 when complemented with other published data) leading to the non-detection of the color/slope-inclination trend, which is known to exist among classicals. Thus, a more complete set of color/slope data would be required for our targets. Only when combining the hot sub-sample from this work and literature we see a non-significant anti-correlation between slope and inclination (see Table 8). We do not find any correlations of the $B-V$, $V-R$ and $V-I$ colors with other parameters.

The apparent H_V vs i anti-correlation in our target sample mentioned in Sect. 2.1 is almost significant (2.7σ) for our hot sub-population (see Table 8).

5.2. Binaries

Binary systems are of particular scientific interest because they provide unique constraints on the elusive bulk composition, whereas all other observational constraints of the composition only pertain to the surface of the object. The sizes of binaries can be constrained based on the relative brightness difference

Table 8. Selected correlation results (see text).

Variables	Sub-sample	Number of data points	Correlation coefficient	Significance	Confidence limit (σ)
D, i	this work	18	$0.69^{+0.14}_{-0.23}$	0.002	3.2
	this work/cold	6	$-0.10^{+0.61}_{-0.54}$	0.8	0.2
	this work/hot	12	$0.82^{+0.10}_{-0.22}$	0.0011	3.3
	this work and prev. works	26	$0.65^{+0.11}_{-0.15}$	0.0004	3.6
	this work/hot and prev. works	20	$0.60^{+0.16}_{-0.24}$	0.005	2.8
D, p_V	this work	18	$-0.76^{+0.11}_{-0.08}$	0.0002	3.7
	this work/cold	6	$-0.40^{+0.68}_{-0.41}$	0.4	0.8
	this work/hot	12	$-0.62^{+0.28}_{-0.18}$	0.03	2.2
	this work and prev. works	26	$-0.59^{+0.16}_{-0.12}$	0.002	3.2
	this work/hot and prev. works	20	$-0.46^{+0.24}_{-0.19}$	0.04	2.1
H_V, i	this work	18	$-0.56^{+0.27}_{-0.19}$	0.015	2.4
	this work/cold	6	$-0.02^{+0.59}_{-0.58}$	1.0	0.03
	this work/hot	12	$-0.74^{+0.45}_{-0.18}$	0.006	2.7
spectral slope, i	this work/hot and prev. works	15	$-0.65^{+0.32}_{-0.19}$	0.011	2.6

of the primary and the secondary components, but only if suitable assumptions about the relative geometric albedo are made. Alternatively, geometric albedos can be constrained under certain assumptions about the relative sizes. The ranges given in the literature are usually based on the following assumptions: i) the primary and secondary objects are spherical, ii) the primary and secondary have equal albedos, and iii) objects have densities within a limited assumed range.

Six of our targets are binaries with known total mass m and brightness difference between the two components ΔV (see Table 9). Assuming the two components to have identical albedos, the latter can be converted into an area ratio and, assuming spherical shape, a diameter ratio $k = D_2/D_1$ (with component diameters D_1 and D_2). Component diameters follow from the measured NEATM diameter D (see Table 6) and D_2/D_1: $D^2 = D_1^2 + D_2^2$ (since D is the area-equivalent system diameter). This leads to a "volumetric diameter" $D' = \frac{(1+k^3)^{1/3}}{\sqrt{1+k^2}} D$. The mass densities $\frac{6m}{\pi D'^3}$ are given in Table 9. Within the uncertainties, the measured bulk densities scatter around roughly 1 g cm^{-3}, consistent with a bulk composition dominated by water ice, as expected for objects in the outer solar system. Significant mass contributions from heavier materials, such as silicates, are not excluded however, and would have to be compensated by significant amounts of macroporosity. The largest object, 120347 Salacia, has a bulk density >1 g cm^{-3}. This could indicate a lower amount of macroporosity for this object, which is subject to significantly larger gravitational self-compaction than our other binary targets.

6. Conclusions

The number of classical TNOs with both the size and the geometric albedo measured radiometrically is increased by eight from 22 to 30. Four other targets, which previously had estimated size ranges from the analysis of binary systems, now have more accurate size estimates. The number of targets observed and analysed within the "TNOs are Cool" program (Müller et al. 2010; Lellouch et al. 2010; Lim et al. 2010; Santos-Sanz et al. 2012; Mommert et al. 2012) is increased by 18 and the observation of 79360 Sila disturbed by a background source in Müller et al. (2010) has been re-observed and analyzed. Furthermore, three targets which earlier had upper and lower limits only based on *Spitzer* data alone (148780 Altjira, 138537 (2000 OK_{67}) and 2001 RZ_{143}) now have accurately estimated diameters and albedos. The new Altjira solution is outside of the previous limits based on *Spitzer* data alone. The three PACS data points near the thermal peak are providing reliable diameter/albedo solutions, but in some cases adding *Spitzer* data, especially the 24 μm data point in the lower-wavelength regime, constrains the solution and allows smaller error bars and more reliable estimates of the beaming parameter. Compared to previous works the size estimates of 119951 (2002 KX_{14}), and 2002 MS_4 have increased. 2002 MS_4 (934 km) is similar in size to 50000 Quaoar and the refined size of 120347 Salacia (901 km) is similar to that of 90482 Orcus. We find a diameter for 2001 KA_{77}, which is approximately half of the previous estimate (Brucker et al. 2009), and a geometric albedo approximately 4 times higher. The largest change in estimated geometric albedo is with 119951 (2002 KX_{14}) from 0.60 to 0.097.

The main conclusions based on accurately measured classical TNOs are:

1. There is a large diversity of objects' diameters and geometric albedos among classical TNOs.
2. The dynamically cold targets have higher (average 0.17 ± 0.04) and differently distributed albedos than the dynamically hot targets (0.09 ± 0.05) in our sample. When extended by seven hot classicals from literature the average is 0.11 ± 0.04.
3. Diameters of classical TNOs strongly correlate with orbital inclination in the sample of targets, whose size and geometric albedo have been accurately measured, i.e. low inclination objects are smaller. We find no clear evidence of an albedo-inclination trend.
4. Our data suggests that geometric albedos of classical TNOs anti-correlate with diameter, i.e. smaller objects possess higher albedos.
5. Our data does not show evidence for correlations between surface colors, or spectral slope, of classical TNOs and their diameters nor with their albedos.
6. We are limited by the small sample size of radiometrically measured accurate diameters/albedos of dynamically cold classicals ($N = 6$) finding no statistical evidences for any correlations.
7. The cumulative size distribution of hot classicals based on the sample of measured sizes in the range of diameters between 100 and 600 km ($N = 11$) has a slope of $q \approx 1.4$.

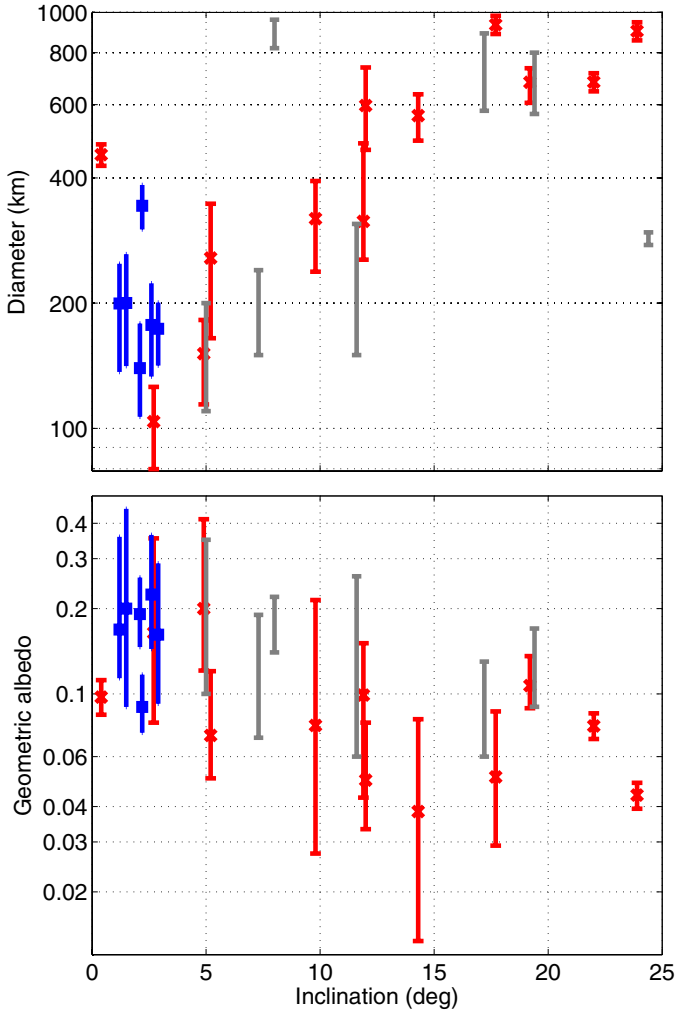

Fig. 7. Radiometric diameter as well as geometric albedo vs inclination. The cold classicals of our sample are marked with blue squares, hot classicals with red crosses and hot classicals from literature with gray points. The high-albedo target 55636 (2002 TX_{300}) is beyond the scale.

Table 9. New density estimates for binaries.

Target	Adopted ΔV^a (mag)	Mass^a ($\times 10^{18}$ kg)	Bulk density (g cm^{-3})
(2001 XR_{254})	0.43	4.055 ± 0.065	$1.4^{+1.3}_{-1.0}$
275809	0.20	4.105 ± 0.038	$1.4^{+1.2}_{-1.3}$
79360	0.12^b	10.84 ± 0.22	0.73 ± 0.28
88611	0.70	2.445 ± 0.032	$1.14^{+0.87}_{-0.91}$
148780	0.23	3.986 ± 0.067	$0.63^{+0.68}_{-0.63}$
120347	2.32	466 ± 22	1.38 ± 0.27

References. [(a)] Grundy et al. (2011). [(b)] Grundy et al. (2012).

8. We determine the bulk densities of six classicals. They scatter around ~1 g cm^{-3}. The high-mass object 120347 Salacia has a density of (1.38 ± 0.27) g cm^{-3}.

Acknowledgements. We thank Chemeda Ejeta for his work in the dynamical classification of the targets of the "TNOs are Cool" program. We acknowledge the helpful efforts of David Trilling in the early planning of this program. Part of this work was supported by the German *DLR* project numbers 50 OR 1108, 50 OR 0903, 50 OR 0904 and 50OFO 0903. M. Mommert acknowledges support trough the DFG Special Priority Program 1385. C. Kiss and A. Pal acknowledge the support of the Bolyai Research Fellowship of the Hungarian Academy of Sciences. J. Stansberry acknowledges support by NASA through an award issued by JPL/Caltech. R. Duffard acknowledges financial support from the MICINN (contract Ramón y Cajal). P. Santos-Sanz would like to acknowledge financial support by the Centre National de la Recherche Scientifique (CNRS). J.L.O. acknowledges support from spanish grants AYA2008-06202-C03-01, P07-FQM-02998 and European FEDER funds.

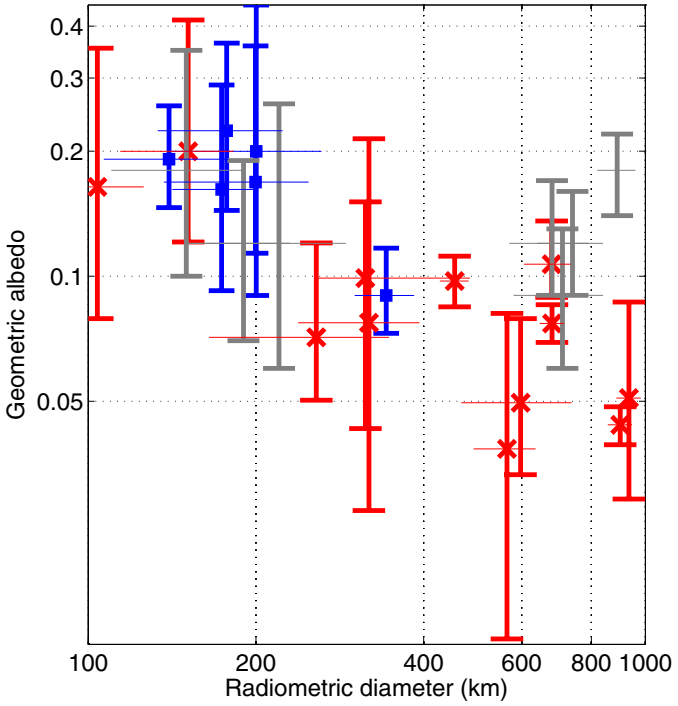

Fig. 8. Geometric albedo vs radiometric diameter (blue triangles = cold classicals, red crosses = hot classicals from our sample, gray = other hot classicals from literature, see Table 7).

References

Altenhoff, W. J., Bertoldi, F., & Menten, K. M. 2004, A&A, 415, 771
Barucci, M. A., Romon, J., Doressoundiram, A., & Tholen, D. J. 2000, AJ, 120, 496
Barucci, M. A., Alvarez-Candal, A., Merlin, F., et al. 2011, Icarus, 214, 297
Batygin, K., Brown, M. E., & Fraser, W. C. 2011, ApJ, 738, 13
Belskaya, I. N., Levasseur-Regourd, A.-C., Shkuratov, Y. G., & Muinonen, K., in The Solar System Beyond Neptune, ed. M. A. Barucci, H. Boehnhardt, D. P. Cruikshank, & A. Morbidelli, 115
Benecchi, S. D., Noll, K. S., Grundy, W. M., et al. 2009, Icarus, 200, 292
Benecchi, S. D., Noll, K. S., Stephens, D. C., et al. 2011, Icarus, 213, 693
Bernstein, G. M., Trilling, D. E., & Allen, R. L. 2004, AJ, 128, 1364
Bessell, M. S., Castelli, F., & Plez, B. 1998, A&A, 333, 231
Boehnhardt, H., Tozzi, G. P., & Birkle, K. 2001, A&A, 378, 653
Bowell, E., Hapke, B., Domingue, D., et al. 1989, in Asteroids II (University of Arizona Press)
Brucker, M. J., Grundy, W. M., Stansberry, J. A., et al. 2009, Icarus, 201, 284
Chiang, E. I., & Brown, M. E. 1999, AJ, 118, 1411
Davies, J. K., Green, S., McBride, N., et al. 2000, Icarus, 146, 253
Delsanti, A. C., Böhnhardt, H., Barrera, L., et al. 2001, A&A, 380, 347
DeMeo, F. E., Fornasier, S., Barucci, M. A., et al. 2009, A&A, 493, 283
Duffard, R., Ortiz, J. L., Thirouin, A., et al. 2009, A&A, 505, 1283
Doressoundiram, A., Peixinho, N., de Berg, C., et al. 2002, AJ, 124, 2279
Doressoundiram, A., Peixinho, N., Doucet, C., et al. 2005, Icarus, 174, 90
Doressoundiram, A., Peixinho, N., Moullet, A., et al. 2007, AJ, 134, 2186
Dotto, E., Perna, D., Barucci, M. A., et al. 2008, A&A, 490, 829
Elliot, J. L., Kern, S. D., Clancy, K. B., et al. 2005, AJ, 129, 1117
Elliot, J. L., Person, M. J., Zuluaga, C. A., et al. 2010, Nature, 465, 897
Engelbracht, C. W., Blaylock, M., Su, K. Y. L., et al. 2007, PASP, 119, 994
Fornasier, S., Barucci, M. A., de Bergh, C., et al. 2009, A&A, 508, 457
Fraser, W. C., & Brown, M. E. 2010, ApJ, 714, 1547
Fraser, W. C., Brown, M. E., & Schwamb, M. E. 2010, Icarus, 210, 944
Fulchignoni, M., Belskaya, I., Barucci, M. A., et al. 2008, in The Solar System Beyond Neptune, ed. M. A. Barucci, H. Boehnhardt, D. P. Cruikshank, & A. Morbidelli, 181

Giorgini, J. D., Yeomans, D. K., Chamberlin, A. B., et al. 1996, BAAS, 28, 1158
Gladman, B., Marsden, B. G., & VanLaerhoven, Ch. 2008, in The Solar System Beyond Neptune, ed. M. A. Barucci, H. Boehnhardt, D. P. Cruikshank, A. Morbidelli, 43
Gordon, K. D., Engelbracht, C. W., & Fadda, D. 2007, PASP, 119, 1019
Grundy, W. M., Noll, K. S., & Stephens, D. C. 2005, Icarus, 176, 184
Grundy, W. M., Noll, K. S., Buie, M. W., et al. 2009, Icarus, 200, 627
Grundy, W. M., Noll, K. S., Nimmo, F., et al. 2011, Icarus, 213, 678
Grundy, W. M., Benecchi, S. D., Rabinowitz, D. L., et al. 2012, Icarus, submitted
Hainaut, O., & Delsanti, A. 2002, A&A, 389, 641, updated data base URL: http://www.eso.org/~ohainaut/MBOSS/, accessed July 2011
Harris, A. W. 1998, Icarus, 131, 291
Harris, A. W. 2006, in Asteroids, Comets, Meteors, ed. D. Lazzaro, S. Ferraz-Mello, & J. A. Fernández, Proc. IAU Symp., 229, 2005
Hayes, D. S. 1985, in IAU Symp. 111, ed. D. S. Hayes, et al., 225
Hovis, W. A., & Callahan, W. R. 1966, J. Opt. Soc. Amer., 56, 639
Jewitt, D., & Luu, J. 1993, Nature, 362, 730
Kenyon, S. J., Bromley, B. C., O'Brien, D. P., & Davis, D. R. 2008, in The Solar System Beyond Neptune, ed. M. A. Barucci, H. Boehnhardt, D. P. Cruikshank, & A. Morbidelli, 293
Kiss, Cs., Klaas, U., & Lemke, D. 2005, A&A, 430, 343
Lagerros, J. S. V. 1996, A&A, 310, 1011
Lebofsky, L. A., & Spencer, J. R. 1989, in Asteroids II, ed. R. P. Binzel, T. Gehrels, & M. S. Matthews (Arizona University Press), 128
Lebofsky, L. A., Sykes, M. V., Tedesco, E. F., et al. 1986, Icarus, 68, 239
Lellouch, E., Kiss, Cs., Santos-Sanz, P., et al. 2010, A&A, 518, L147
Levison, H. F., & Stern, S. A. 2001, AJ, 121, 1730
Levison, H. F., Morbidelli A., VanLaerhoven, Ch., et al. 2008, Icarus, 196, 258
Lim, T. L., Stansberry, J., Müller, Th., et al. 2010, A&A, 518, L148
Matson, D. L., 1971, Ph.D. Thesis, California Institute of Technology
Mommert, M., Harris, A. W., Kiss, C., et al. 2012, A&A, 541, A93
Morbidelli, A., Levison, H. F., & Gomes, R., 2008, in The Solar System Beyond Neptune, ed. M. A. Barucci, H. Boehnhardt, D. P. Cruikshank, & A. Morbidelli, 275
Moro-Martín, A., Wyatt, M. C., Malhotra, R., & Trilling, D. E. 2008, in The Solar System Beyond Neptune, ed. M. A. Barucci, H. Boehnhardt, D. P. Cruikshank, & A. Morbidelli, 465
Mueller, M., Delbo, M., Hora, J. L., et al. 2011, AJ, 141, 109
Müller, T. G., & Lagerros, J. S. V. 1998, A&A, 338, 340
Müller, T. G., Lellouch, E., Böhnhardt, H., et al. 2009, Earth Moon and Planets, 105, 209
Müller, Th., Lellouch, E., Stansberry, J., et al. 2010, A&A, 518, L146
Noll, K. S., Grundy, W. M., Stephens, D. C., et al. 2008, Icarus, 194, 758
Osip, D. J., Kern, S. D., & Elliot, J. L. 2003, Earth, Moon, Planets, 92, 409
PACS AOT Release Note: PACS Photometer Point/Compact Source Mode 2010, PICC-ME-TN-036, Version 2.0, custodian Th. Müller, URL: http://herschel.esac.esa.int/twiki/bin/view/Public/PacsCalibrationWeb
PACS photometer – Point Source Flux Calibration 2011, PICC-ME-TN-037, Version 1.0, URL: http://herschel.esac.esa.int/twiki/bin/view/Public/PacsCalibrationWeb
PACS photometer point spread function 2010, PICC-ME-TN-033, Version 1.01, custodian D. Lutz, http://herschel.esac.esa.int/twiki/bin/view/Public/PacsCalibrationWeb
Peixinho, N., Boehnhardt, H., Belskaya, I., et al. 2004, Icarus, 170, 153
Peixinho, N., Lacerda, P., & Jewitt, D. 2008, AJ, 136, 1837
Perna, D., Barucci, M. A., & Fornasier, S. 2010, A&A, 510, A53
Petit, J.-M., Holman, M. J., Gladman, B., et al. 2006, MNRAS, 365, 429
Petit, J.-M., Kavelaars, J. J., Gladman, B., & Loredo, T. 2008, in The Solar System Beyond Neptune, ed. M. A. Barucci, H. Boehnhardt, D. P. Cruikshank, & A. Morbidelli, 71
Petit, J.-M., Kavelaars, J. J., Gladman, B., et al. 2011, AJ, 142, 142
Pilbratt, G. L., Riedinger, J. R., & Passvogel, T. 2010, A&A, 518, L1
Poglitsch, A., Waelkens, C., Geis, N., et al. 2010, A&A, 518, L2
Rabinowitz, D. L., Schaefer, B. E., & Tourtellotte, S. W. 2007, AJ, 133, 26
Rieke, G. H., Young, E. T., Engelbracht, C. W., et al. 2004, ApJS, 154, 25
Romanishin, W., & Tegler, S. C. 2005, Icarus, 179, 523
Santos-Sanz, P., Ortiz, J. L., Barrera, L., & Boehnhardt, H. 2009, A&A, 494, 693
Santos-Sanz, P., Lellouch, E., Fornasier, S., et al. 2012, A&A, 541, A92
Schmitt, B., Quirico, E., Trotta, F., & Grundy, W. M. 1998, in solar system Ices, Based on reviews presented at the international symposium "Solar system ices" held in Toulouse, France, on March 27–30, 1995, ed. B. Schmitt, C. de Bergh, & M. Festou (Dordrecht Kluwer Academic Publishers), Astrophys. Space Sci. Lib. (ASSL) Ser., 227, 199
Sheppard, S. S. 2007, AJ, 134, 787
Sheppard, S. S., & Jewitt, D. C. 2002, AJ, 124, 1757
Spearman, C. 1904, Am. J. Psychol., 57, 72
Spencer, J. R., Lebofsky, L. A., & Sykes, M. V. 1989, Icarus, 78, 337
Stansberry, J. A., Pisano, D. J., & Yelle, R. V. 1996, Planet. Space Sci., 44, 945
Stansberry, J., Gordon, K. D., Bhattacharya, B., et al. 2007, PASP, 119, 1038
Stansberry, J., Grundy, W., Brown, M., et al. 2008, in The Solar System Beyond Neptune, ed. M. A. Barucci, H. Boehnhardt, D. P. Cruikshank, & A. Morbidelli, 161
Stansberry, J. A., Grundy, W. G., Müller, M., et al. 2012, Icarus, accepted, DOI:10.1016/j.icarus.2012.03.029
Stetson, P. B. 1987, PASP, 99, 191
Tegler, S. C., & Romanishin, W. 2000, Nature, 407, 979
Thirouin, A., Ortiz, J. L., & Duffard, R. 2010, A&A, 522, A93
Thirouin, A., Ortiz, J. L., Campo Bagatin, A., et al. 2012, MNRAS, submitted
Trujillo, C. A., & Brown, M. E. 2002, ApJ, 566, L125
Tsiganis, K., Gomes, R., Morbidelli, A., & Levison, H. F. 2005, Nature, 435, 459
Veeder, G. J., Hanner, M. S., & Matson, D. L. 1989, AJ, 97, 1211
Werner, M. W., Roellig, T. L., Low, F. J., et al. 2004, ApJS, 154, 1
Wyatt, M. C. 2008, ARA&A, 46, 339